

Variation in the Stellar Initial Mass Function from the Chromospheric Activity of M Dwarfs in Early-type Galaxies

Pieter van Dokkum¹ and Charlie Conroy² Astronomy Department, Yale University, 52 Hillhouse Ave., New Haven, CT 06511, USA Harvard-Smithsonian Center for Astrophysics, 60 Garden Street, Cambridge, MA 02138, USA Received 2021 June 28; revised 2021 September 20; accepted 2021 September 23; published 2021 December 9

Abstract

Mass measurements and absorption-line studies indicate that the stellar initial mass function (IMF) is bottom-heavy in the central regions of many early-type galaxies, with an excess of low-mass stars compared to the IMF of the Milky Way. Here we test this hypothesis using a method that is independent of previous techniques. Low-mass stars have strong chromospheric activity characterized by nonthermal emission at short wavelengths. Approximately half of the UV flux of M dwarfs is contained in the $\lambda 1215.7$ Ly α line, and we show that the total Ly α emission of an early-type galaxy is a sensitive probe of the IMF with a factor of \sim 2 flux variation in response to plausible variations in the number of low-mass stars. We use the Cosmic Origins Spectrograph on the Hubble Space Telescope to measure the Ly α line in the centers of the massive early-type galaxies NGC 1407 and NGC 2695. We detect Ly α emission in both galaxies and demonstrate that it originates in stars. We find that the Ly α to *i*-band flux ratio is a factor of 2.0 ± 0.4 higher in NGC 1407 than in NGC 2695, in agreement with the difference in their IMFs as previously determined from gravity-sensitive optical absorption lines. Although a larger sample of galaxies is required for definitive answers, these initial results support the hypothesis that the IMF is not universal but varies with environment.

Unified Astronomy Thesaurus concepts: Early-type galaxies (429); Initial mass function (796); Ultraviolet astronomy (1736); Galaxy formation (595)

1. Introduction

The question whether the stellar initial mass function (IMF) is universal or varies with galactic environment is of fundamental importance for many areas of astrophysics. Limits on, or evidence of, IMF variation inform models for star formation (Krumholz 2011; Hopkins 2012) and would lead to new, more accurate calibrations of the masses and star formation rates of galaxies (see, e.g., Chruślińska et al. 2020). This question is not yet settled, despite many years of efforts and an ever-increasing wealth of observations of star clusters in the Milky Way and of external galaxies (see Bastian et al. 2010, for a review). To this day, almost all studies of galaxy formation and evolution assume that the IMF throughout the universe is universal, from the highest redshifts to the present epoch, from the lowest to highest metallicities, and from the most intense starbursts to the lowest levels of star formation. This universal form is taken to be the Kroupa (2001) or Chabrier (2003) form, which has a power-law slope at high masses and a turnover at low masses. This IMF is a good fit to star clusters in the Milky Way.

Perhaps the most persistent claims for a varying IMF have come from studies of the central regions of the most massive galaxies in the universe. As discussed in the recent review by Smith (2020), the evidence for a bottom-heavy stellar mass function in those environments has come from two independent directions. First, there seems to be more mass than can be accounted for by the combination of the expected amount of dark matter plus a stellar population with a Milky Way–like IMF. This mass discrepancy has been identified using both dynamics (Cappellari et al. 2012) and strong lensing (Treu et al. 2010). Second, detailed spectroscopic studies have claimed to see evidence for subtle gravity-sensitive absorption features indicative of the presence of large numbers of M dwarfs (e.g.,

van Dokkum & Conroy 2010; Conroy & van Dokkum 2012b; Spiniello et al. 2012; La Barbera et al. 2013; Lyubenova et al. 2016). This M-dwarf enhancement seems to be restricted to the centers of the galaxies (Martín-Navarro et al. 2015; La Barbera et al. 2016; Davis & McDermid 2017; van Dokkum et al. 2017).

These results are controversial. The interpretation of the masses requires assumptions about the orbital structure of the galaxies and the dark matter distribution, and the interpretation of the spectra requires exquisite modeling of the abundance patterns and a host of other parameters. Furthermore, although the interpretation of IMF variation has survived some key tests (e.g., a differential comparison to globular clusters; van Dokkum et al. 2011), it has struggled in others. Smith (2014) showed that there is no correlation between the mass excess from dynamics and the M-dwarf excess derived from spectroscopy for individual galaxies. It was later demonstrated that this can largely be explained by aperture effects (Lyubenova et al. 2016; van Dokkum et al. 2017), but even when these are accounted for, the scatter between the two techniques is larger than the formal uncertainties. Smith et al. (2015) and Newman et al. (2017) analyze several nearby strong lenses with very small projected Einstein radii. They find that the three mass constraints (lensing, dynamics, and absorptionline spectroscopy) are inconsistent at the 1σ – 2σ level, unless the low-mass cutoff of the IMF is adjusted. A different issue has arisen in studies of distant galaxies. In marked contrast to measurements in the nearby universe, the kinematics of massive galaxies at $z \sim 2$ appear to rule out bottom-heavy IMFs, as then the total stellar masses of the galaxies would exceed their dynamical masses (van de Sande et al. 2013; Esdaile et al. 2021). However, this apparent discrepancy may reflect systematic errors in the dynamical masses of the galaxies, caused by structural evolution from disk-like at $z \sim 2$ to dynamically hot systems at z = 0 (see van der Wel et al. 2011;

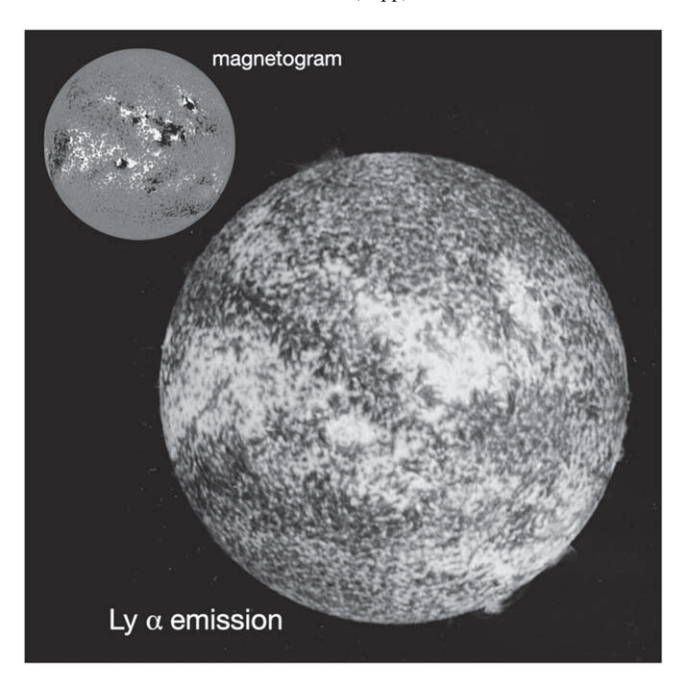


Figure 1. The Sun in the light of the Ly α line, as observed with the Multi-Spectral Solar Telescope Array on 1991 May 13 (Allen et al. 1997). The inset shows the solar magnetogram on the same date. The Ly α emission is dominated by the chromospheric network and plages.

Toft et al. 2017; Bezanson et al. 2018; Newman et al. 2018; Mendel et al. 2020). Future studies of the spatially resolved kinematics of massive early-type galaxies at $z \sim 2$ with the James Webb Space Telescope will shed more light on this issue.

A way to break the impasse is to use new information that is independent from the methods that have been employed over the past decade. The ideal method detects light directly from low-mass stars, is not strongly correlated with other parameters such as metallicity, and has sufficient sensitivity to IMF variations to distinguish Milky Way-like IMFs from Salpeterlike (Salpeter 1955) IMFs. A method that satisfies all these requirements is to measure the mean stellar activity level in galaxies. Stellar activity is a broad term used to indicate behavior that deviates from steady-state balance of the transfer of radiative and convective energy from the stellar interior into its atmosphere (e.g., Linsky 2017). Activity can refer to flaring behavior or the heating of chromospheres in the outer atmospheres of stars. It is observed to be confined to cool stars with convective envelopes and is believed to be in some way connected to the presence of magnetic fields (see Hall 2008, for a review). Chromospheric activity is particularly high in M dwarfs, which can have flares that are 10⁴ times more luminous than those on Sun-like stars (Joy & Abt 1974; Osten et al. 2016). The activity is known to decrease with rotation period, and therefore likely with age (Skumanich 1972; Pallavicini et al. 1981; Giampapa & Liebert 1986; Astudillo-Defru et al. 2017; Kiman et al. 2021); however, even the most slowly rotating M dwarfs have substantial activity (Reiners & Basri 2007; France et al. 2020; Diamond-Lowe et al. 2021).

Recently the chromospheric activity of low-mass stars has received significant attention in the context of the habitability of planets orbiting M dwarfs (e.g., Segura et al. 2010; Shkolnik & Barman 2014; Shields et al. 2016; Loyd et al. 2018), but it can also be used as a fingerprint to identify and count such stars in distant galaxies. The activity is manifested in far-UV (FUV)

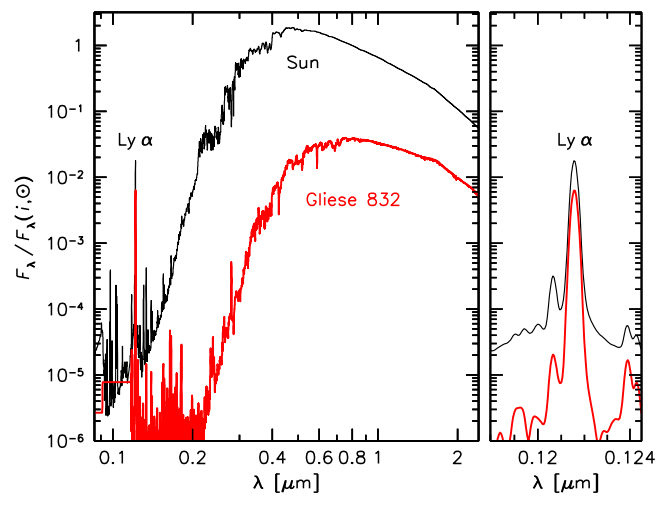


Figure 2. Comparison of spectra of the Sun and the M dwarf Gliese 832, in units of the solar *i*-band luminosity and smoothed to the same spectral resolution. This comparison illustrates the fact that the average $\text{Ly}\alpha/i$ band ratio is much higher in M dwarfs than in Sun-like stars.

continuum emission and a large number of emission lines (Vernazza et al. 1981; Linsky et al. 2012). Some of these lines are in the optical, in particular $H\alpha$, $Ca \, II \, H + K$, and the $Ca \, II$ triplet, but the majority lie in the ultraviolet. The dominant line is $Ly\alpha$ at $\lambda=1215.7\, \mathring{A}$, which traces both the chromospheric network and plages (see Figure 1). As shown in France et al. (2013), this single line composes approximately half of the total flux of M dwarfs in the wavelength range $1150-3100\,\mathring{A}$.

The IMF test that we propose is to measure the strength of Ly α emission in the cores of early-type galaxies, normalized by the overall galaxy flux (measured at a wavelength where the light is dominated by stars around the turnoff mass, such as the iband), and determine whether this Ly α/i ratio correlates with the excess of low-mass stars as independently derived from optical absorption-line spectroscopy. This ratio (which has the units of an equivalent width) is much more sensitive to variations in the number of low-mass stars than the equivalent widths of optical lines. We illustrate this point in Figure 2, which shows a comparison between the spectrum of the M2 dwarf Gliese 832 and that of the Sun. The Gliese 832 spectrum was obtained from the MUSCLES database³ (France et al. 2016; Loyd et al. 2016; Youngblood et al. 2016). The solar spectrum is the irradiance reference spectrum from the 2008 Whole Heliosphere Interval campaign⁴ (Chamberlin et al. 2008; Woods et al. 2009). The spectra were smoothed to a common resolution of $\sigma = 300 \text{ km s}^{-1}$. The bolometric luminosity of Gliese 832 is a factor of \approx 30 lower than that of the Sun, but its Ly α luminosity differs by only a factor of ≈ 2 .

In this paper we put this idea in practice. In Section 2 we generate model predictions for the Ly α/i ratio $W_{\text{Ly}\ \alpha}^i$ using stellar population synthesis techniques. This is facilitated by recent work on stellar activity in the context of the habitability of exoplanets. We then describe in Section 3 new Hubble Space Telescope (HST) Cosmic Origin Spectrograph (COS) observations of two early-type galaxies. The two galaxies, NGC 1407 and NGC 2695, have very similar ages and

 $^{^3}$ The database was accessed through https://archive.stsci.edu/prepds/muscles/. Version 2.2 was used, with Ly α reconstructed to correct for ISM absorption.

⁴ Version 2, obtained from https://lasp.colorado.edu/lisird/data/whi_ref_spectra.

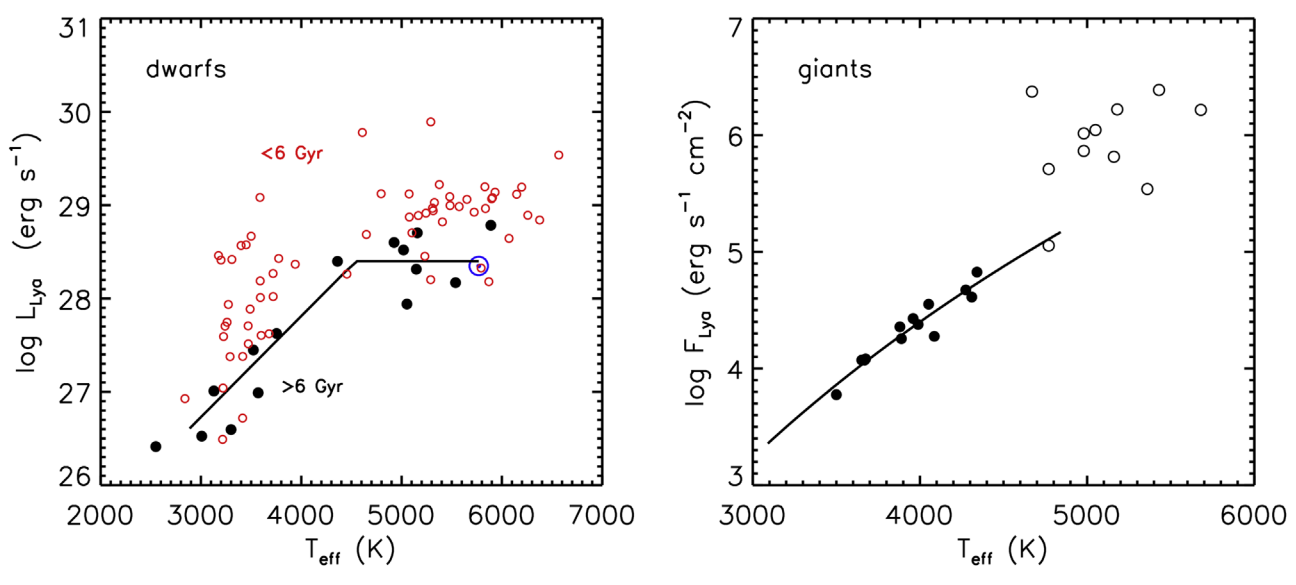


Figure 3. Observations of Ly α emission from dwarfs (left panel, plotted as integrated luminosity) and giants (right panel, plotted as surface flux). In the left panel, stars are color-coded by whether they are younger or older than 6 Gyr. Dwarf data are from the compilation in Linsky et al. (2020). The Sun is shown as a blue open circle. The solid lines indicate our adopted model relations for the dwarf and giant sequences. For the latter, the solid line extends over a temperature range relevant for the giant branch of an old solar-metallicity stellar population. In the right panel, data from Wood et al. (2005) are shown as open symbols, while the cool giant data from Wood et al. (2016) are shown as filled symbols.

abundance patterns but a different IMF according to optical absorption-line spectroscopy (see van Dokkum et al. 2017). The measurement of $W_{\text{Ly}\ \alpha}^i$ in the two galaxies is presented in Section 4. In Section 5 the two data points are compared to the model predictions of Section 2. We end with a concluding section (Section 6).

2. Modeling the Expected Ly α Emission

2.1. Model Ingredients

We compute model stellar populations via the standard stellar population synthesis technique:

$$L_{\rm SSP} = \int \phi(m) \ l(m) dm, \tag{1}$$

where $\phi(m)$ is the IMF, l(m) is the stellar luminosity (e.g., monochromatic or bolometric) as a function of stellar mass, and $L_{\rm SSP}$ is the resulting integrated luminosity for a simple stellar population (SSP). The luminosity-mass relation, l(m), is usually determined by stellar evolution models (isochrones). The above equation is implicitly a function of age and metallicity because the luminosity-mass relation depends on age and metallicity.

In this work we use MIST isochrones, which cover a wide range in age and metallicity and have been extensively calibrated to observations (Choi et al. 2016). We also employ bolometric corrections provided as part of the MIST database in order to determine fluxes in various passbands. We consider both the Kroupa (2001) IMF as the reference "Milky Way" IMF and power-law IMFs with index γ , where $\gamma=2.35$ is the canonical Salpeter IMF. The IMF parameter $\alpha_{\rm IMF}$ is defined as the mass-to-light ratio for a given IMF divided by the mass-to-light ratio appropriate for a Kroupa IMF. For reference, the Salpeter IMF has $\alpha_{\rm IMF}=1.5$. Here we follow Conroy & van Dokkum (2012a) in the treatment of the IMF and computation of the total stellar masses. In particular, we fix the IMF slope above 1 M_{\odot} to the Salpeter value, as those stars are no longer

shining in the old stellar systems of interest to us. We also add stellar remnants (white dwarfs, neutron stars, and black holes) into the total mass budget following Conroy et al. (2009).

In order to build a stellar population model of Ly α , we have adopted an empirical approach, owing to the lack of a solid theoretical foundation for the behavior of stellar activity and chromospheric emission in stars.

For dwarf stars we use the compilation from Linsky et al. (2020). These authors tabulate stellar parameters, ages, and Ly α fluxes for 79 stars. The resulting relation between Ly α luminosity and $T_{\rm eff}$ is shown in the left panel of Figure 3. The solar data are from Woods et al. (2000). It is well known that there is a relation between stellar activity and age such that as stars age their activity decreases. As we are interested in modeling old stellar populations, we focus on the subset of dwarf stars with ages > 6 Gyr in order to define the resulting Ly $\alpha - T_{\rm eff}$ relation. The solid line in Figure 3 shows the final model for dwarfs, which is defined as log Ly $\alpha = 23.48 + 0.0011T_{\rm eff}$ for $T_{\rm eff} \le 4470$ K and log Ly $\alpha = 28.4$ for $T_{\rm eff} > 4470$ K.

Data for giants were collected from two sources. Wood et al. (2005) measured Ly α surface fluxes for individual stars and also measured relations between Ly α and Mg II fluxes. Wood et al. (2016) provided only Mg II fluxes, which we then converted to Ly α fluxes based on the Wood et al. (2005) relation. These data are shown in the right panel of Figure 3. The solid line is the result of combining the Mg II– $T_{\rm eff}$ relation from Wood et al. (2016) with the Ly α –Mg II relation from Wood et al. (2005), resulting in log $F_{\rm Ly}$ α = 9.29 log $T_{\rm eff}$ – 29.08 erg s⁻¹ cm⁻². The solid line spans the temperature range from the base to the tip of the red giant branch for an old solar-metallicity population. The warmer G-type giants are not found in old stellar populations and so are excluded from the model.

The reader will notice different units for the Ly α data used in the dwarf and giant samples—luminosities versus surface fluxes. Ideally the latter would be used throughout, as it is likely more fundamental. For example, holding all other parameters fixed, a larger star should have a larger Ly α

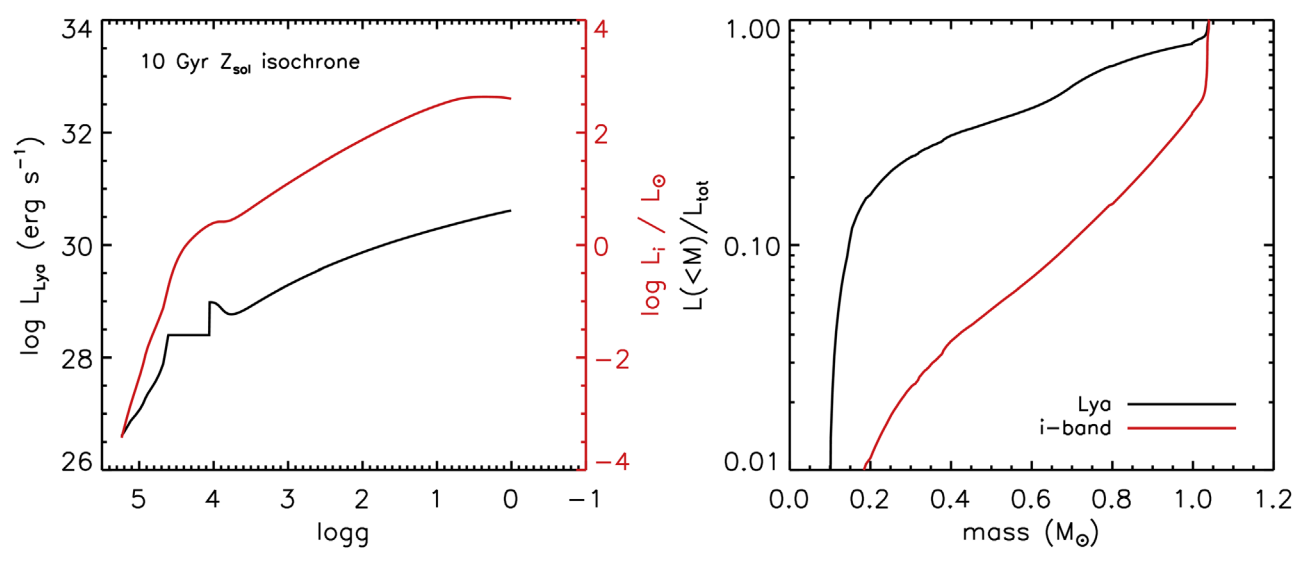


Figure 4. Left panel: model Ly α (black) and *i*-band (red) luminosities for a 10 Gyr solar-metallicity isochrone as a function of surface gravity (log g). Notice that the giant-to-dwarf luminosity ratio is much larger in the *i*-band luminosity than in Ly α . Right panel: fractional contribution to the total integrated Ly α and *i*-band luminosity as a function of stellar mass, assuming a Kroupa IMF. As is well known, low-mass stars (e.g., $< 0.4~M_{\odot}$) contribute only a few percent to the total *i*-band flux. Remarkably, such stars contribute $\approx 30\%$ of the total integrated Ly α emission.

luminosity. Indeed, for the giants, the modeling of the Ly α luminosity is computed in exactly this way: at a given location along the isochrone we are provided the stellar temperature and radius; the temperature is used to define the surface flux, and the radius is employed to compute the integrated luminosity.

For the dwarfs we take a slightly different approach owing in part to the well-known fact that stellar models predict M-dwarf radii that are $\approx 5\%$ smaller than observations (see Choi et al. 2016, for the comparison with MIST isochrones). We adopt the dwarf luminosities (rather than surface fluxes) as fundamental and assume that the sample of dwarfs used to create the relation in Figure 3 is based on solar-metallicity stars (a good assumption since the stars are all very near to the Sun). In order to compute models at different metallicities, where the stellar radii will be different at fixed temperature, we scale the empirical relation by the ratio of nonsolar to solar-metallicity squared radii. In short, we are assuming that the models predict the correct relative change in stellar radii as a function of metallicity.

In this work we assume that the relations adopted in Figure 3 are independent of age and metallicity (modulo the scaling for the dwarfs just described). For the giants, the activity is believed to be sourced by the convective motions of the envelope with no expected dependence on age. As we have discussed above, the activity of dwarfs is strongly age dependent, though we have argued that the data favor a stable relation for ages > 6 Gyr. There are no data to test the metallicity dependence of these relations, and so we have little option but to assume no dependence in the model. Future observations over a wider range of ages and metallicities would be valuable.

We have now assembled the ingredients necessary to construct a stellar population model for Ly α . The relations shown in Figure 3, along with stellar isochrones, allow for the construction of an Ly α luminosity—mass relation, which, along with Equation (1) and an assumed IMF, provides an integrated Ly α luminosity for a particular stellar population. In later sections we will also make use of the integrated *i*-band luminosity. This is computed via Equation (1) with the

luminosity-mass relation tabulated directly in the MIST isochrones.

2.2. Expected IMF Dependence of $W^i_{\rm Ly~\alpha}$, the Ly α 1-band Flux Ratio

With the stellar population model ingredients in place, we can now explore the predicted behavior of Ly α as a function of age, metallicity, and the IMF.

To build intuition, we begin with Figure 4. In the left panel we show the predicted model Ly α and *i*-band luminosities (L_i) as a function of log g for a 10 Gyr solar-metallicity population with a Kroupa IMF. The lines show only the main-sequence and first-ascent giants for clarity. The small bump at $\log g \approx 4$ for the Ly α predictions is a consequence of our adopted surface flux- $T_{\rm eff}$ relation for the giants and is of no practical consequence for the model predictions. The right panel shows the cumulative luminosity contribution as a function of stellar mass. The behavior for L_i is well known–giants are much more luminous than dwarfs, and G and K dwarfs are in turn much more luminous than M dwarfs. These facts imply that the lowmass stars, e.g., $<0.4 M_{\odot}$, compose only a few percent of the integrated light. It is this fact that has made IMF measurements based on integrated-light optical-near-IR spectroscopy so challenging (see, e.g., Conroy & van Dokkum 2012a, 2012b).

The behavior of the Ly α model is dramatically different. The left panel of Figure 4 shows that the ratio of Ly α for the lowest and highest log g stars is approximately $100 \times$ smaller than for L_i . This implies that the low-mass stars contribute a much larger fraction of the total model Ly α luminosity, as shown in the right panel. For a Kroupa IMF, stars with <0.4 M_{\odot} contribute 30% of the integrated Ly α luminosity. Photospheric emission at any wavelength provides nowhere near this level of sensitivity to low-mass stars. This result quantitatively demonstrates the unique sensitivity of stellar activity indicators as a probe of the low-mass population in integrated stellar populations.

The overall predicted flux level from a model population depends on both the intrinsic stellar population parameters, such as age, metallicity, and IMF, and the overall number of

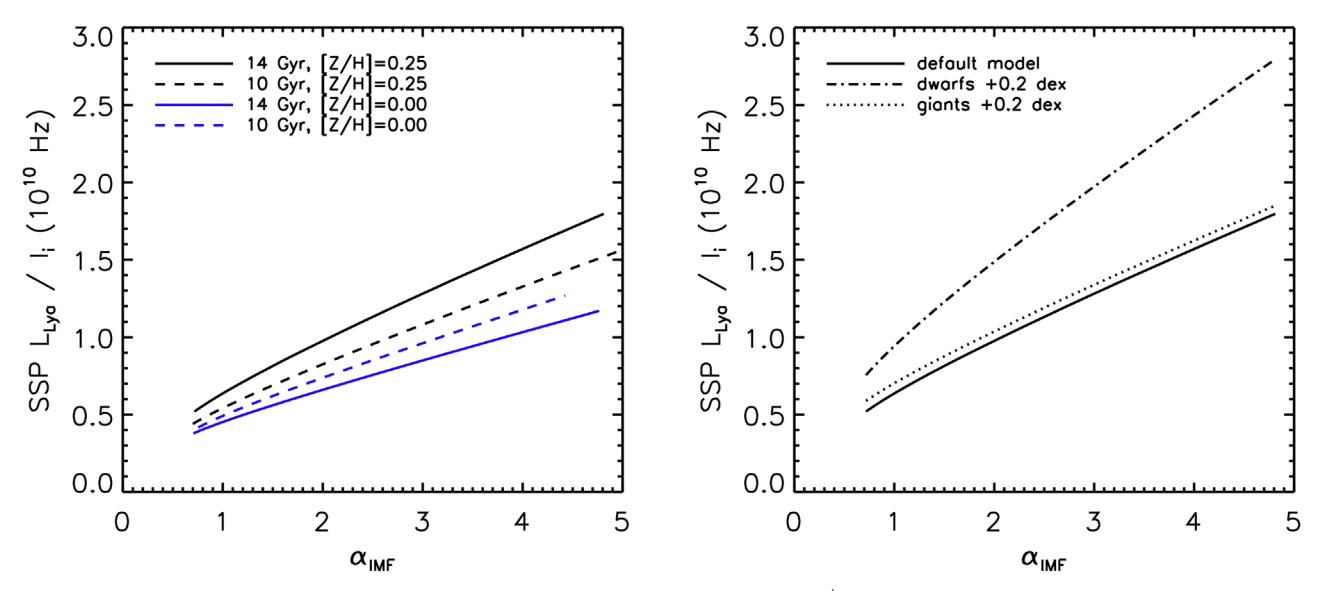


Figure 5. Left panel: stellar population model predicted ratio of the Ly α to *i*-band luminosity ratio $W^i_{\rm Ly\,\alpha}$ as a function of the IMF parameter, $\alpha_{\rm IMF}$, where $\alpha_{\rm IMF}=1$ represents a Kroupa (2001) IMF. Results are shown for two ages (10 and 14 Gyr) and two metallicities ([Z/H]] = 0.00 and 0.25). Right panel: same as the left panel, now showing variations in the underlying stellar population model with respect to a 14 Gyr, [Z/H] = 0.25 model. The base model is for the quiescent state and does not take flares into account. Dotted—dashed and dotted lines in the right panel show the effect of increasing by 0.2 dex (60%) the overall Ly α luminosity of dwarfs and giants, respectively. The model predictions are much more sensitive to the details of the dwarf model than the giant model.

stars (i.e., the total stellar mass). In cases where we are primarily interested in the former quantities, it is common to construct ratios of luminosities (e.g., colors) in order to remove the effect of the overall number of stars. Here we proceed in a similar fashion and consider $W^i_{\rm Ly~\alpha}$, the ratio of Ly α luminosity to the *i*-band luminosity. As the latter is a luminosity density, the unit of this ratio is similar to an equivalent width, with units of Hz.

Figure 5 shows the predicted $W_{\rm Ly}^i$ ratio for model stellar populations as a function of the IMF parameter $\alpha_{\rm IMF}$. The IMF is assumed to be a single power law with index γ in the range 1.2–3.3. In the left panel, results are shown for two ages (10 and 14 Gyr) and two metallicities ([Z/H] = 0.0 and 0.25)—parameters relevant for massive quiescent galaxies. As expected, higher values of $\alpha_{\rm IMF}$ result in larger values of the ratio. At fixed IMF, higher metallicities result in a larger ratio.

A complication is the effect of flares, which we have not included in our model. Flares empirically follow a power-law relation between their occurrence rate and energy such that more energetic flares are less common (rate $\propto E^{-\alpha}$). Loyd et al. (2018) find that for FUV flares the power-law index is less than 1 for inactive M dwarfs ($\alpha \approx 0.74$), which implies that the rarer, more energetic flares could dominate the total energy output of a population. As an example, Diamond-Lowe et al. (2021) find in their FUV observations of LHS 3844 a single flare with energy 10× the quiescent level and an occurrence rate of $\approx 2\%$. If these flare properties were uniformly applied to our Ly α dwarf model, it would result in an increase in the Ly α fluxes of 0.07 dex. We can use the frequency distribution from Loyd et al. to scale the result for LHS 3844 to higher energies: a flare 100× more energetic than the quiescent state would occur with a rate of 0.3%, and if applied uniformly to all stars, it would enhance the model Ly α fluxes by 0.12 dex. We note that the Ly α line is optically thick and may not respond to flares in the same way as the FUV emission studied by Loyd et al. (2018). In the case of the Sun, there is evidence that the Ly α increase during flares is smaller than that of the continuum and of optically thin lines (Milligan et al. 2020; Chamberlin et al. 2020). While direct Ly α measurements of low-mass stars during flares are needed to better quantify the flare contribution, the basic point here is that a reasonable range of flare rates and energies could result in an enhancement in the dwarf model in the range of 0.1–0.2 dex, with 0.2 dex probably the maximum contribution.

In the right panel we show the sensitivity of the model predictions to flares. The variations are with respect to a reference model of 14 Gyr and [Z/H] = 0.25. We increase by 0.2 dex the Ly α - $T_{\rm eff}$ relations shown in Figure 3, separately for dwarfs and giants. Unsurprisingly in light of Figure 4, the model predictions are quite insensitive to the details of the giant model. In contrast, the model is sensitive to the dwarf model, as expected.

3. FUV Spectra of NGC 1407 and NGC 2695

3.1. HST/COS Program

We obtained HST/COS FUV spectra of two galaxies, NGC 1407 and NGC 2695, in a pilot program to measure Ly α emission in the cores of massive early-type galaxies. These galaxies were the subject of an in-depth study of IMF variation in Section 5.1 of van Dokkum et al. (2017). Although that paper focuses on radial gradients, that particular section is a stand-alone analysis of the absorption-line spectra of these two galaxies. The reason is that the centers of these galaxies have nearly identical stellar population properties *except* the IMF (and their velocity dispersions). Their Ca, Fe, Ti, C, O, Mg, N, and Na abundances are all within $\lesssim 0.05$ dex of each other, and

⁵ Truth be told, we were actually hoping to detect other FUV lines, such as Si II and C IV. We had estimated the expected fluxes of these lines using a (probably erroneous) tentative detection of Ca H + K emission in NGC 1407 and concluded that they could be detected at $\sim 5\sigma$ significance if that galaxy indeed has a bottom-heavy IMF. In fact, the only line that gives any hope of a detection is Ly α , but we had not yet done the modeling of Section 2 when we wrote the HST proposal. We acknowledged in the proposal that we really did not know what to expect and warned the TAC that a likely outcome would be that no lines would be detected for either galaxy. We are grateful to the TAC for taking a chance on our proposal.

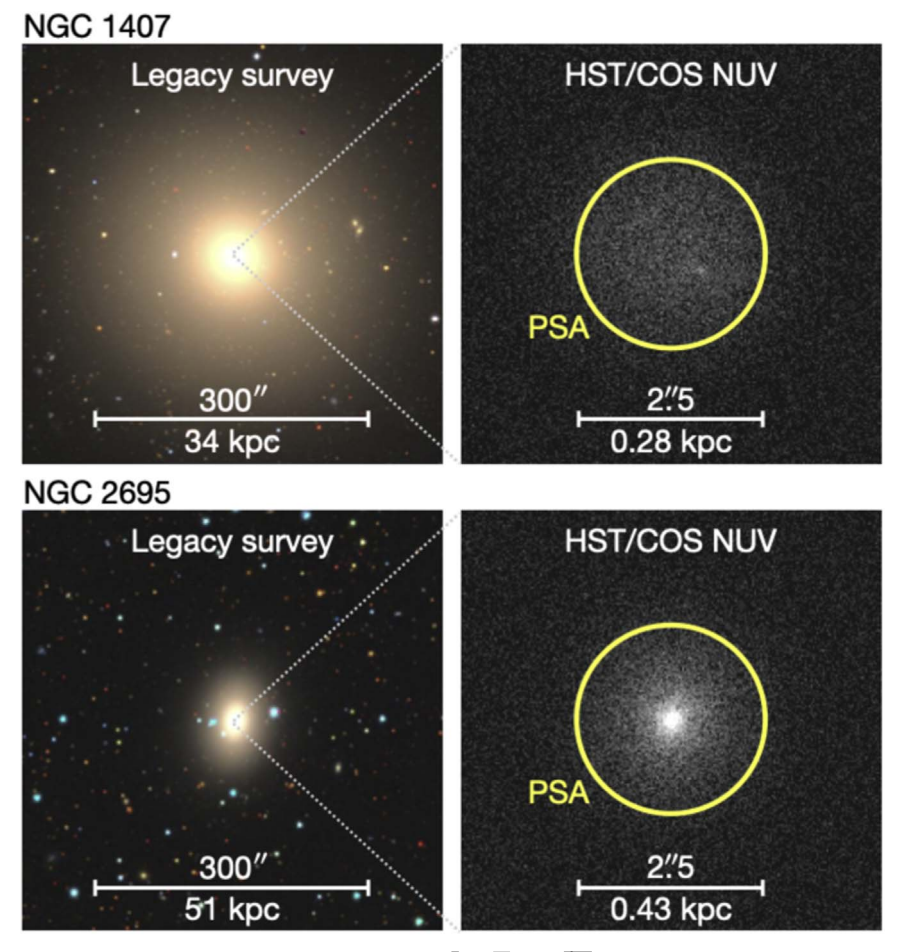


Figure 6. Direct images of NGC 1407 and NGC 2695 in the COS NUV channel ($\lambda_{\rm eff} \approx 2300$ Å), obtained through the PSA after a blind offset from a nearby star. NGC 1407 has a near-constant surface density core, whereas NGC 2695 has a dense just-resolved nucleus.

their best-fitting ages are also nearly identical (13.3 Gyr for NGC 1407 and 13.7 Gyr for NGC 2695). However, their best-fitting IMFs are quite different: $\alpha_{\rm IMF} = 3.29^{+0.23}_{-0.25}$ for NGC 1407 and $\alpha_{\text{IMF}} = 1.93^{+0.22}_{-0.19}$ for NGC 2695. In Figure 15 of van Dokkum et al. (2017) it is shown that it is not possible to fit the spectra of both galaxies with models that do not include IMF variation.

These galaxies were therefore the clear choice for our proposed COS program. A larger sample than two would obviously be preferred, but these particular galaxies can already deliver important insights because their stellar populations are so similar. Differences in $W^i_{\text{Ly}\alpha}$ are not a priori expected, unless they are in fact due to IMF variations. The galaxies also have no known dust or gas that could complicate the Ly α measurement, and their radial velocities are sufficiently large that their Ly α emission is well separated from geocoronal emission.

3.2. Observations

FUV spectra of NGC 1407 and NGC 2695 were obtained in the Cycle 27 program GO-15852, on 2020 May 21 and 23 (NGC 2695) and 2020 August 10 and 11 (NGC 1407). Each galaxy was observed for four orbits. The four orbits were split into two visits of two orbits each. At the beginning of each visit

an acquisition was performed to place the center of the galaxy in the center of the 2"5-diameter primary science aperture (PSA). As the targets are faint and spatially extended, the acquisition required "blind" offsets from nearby stars. We devised a procedure where we first acquire the star, then perform an offset to the target, obtain a 300 s direct near-UV (NUV) image through the PSA, and finally obtain exposures with the grating for the remainder of the first orbit and the entirety of the second orbit. The primary goal of the direct images is to verify that the galaxies are properly centered within the PSA. Furthermore, knowledge of the spatial distribution of the UV light aids in the interpretation of the spectra, particularly since no HST imaging (at any wavelength) has previously been obtained for NGC 2695.

The acquisition images show no detectable offsets, with the caveat that the center is somewhat difficult to measure for NGC 1407. During the imaging exposures, the wavelength calibration lamp was deliberately turned on, creating a bright spot that can be used to align images taken in different visits. The aligned and combined images are shown in Figure 6. The NUV channel has broad wavelength coverage from approximately 1750 to 3000 Å, with $\lambda_{\rm eff} \approx 2300$ Å. The galaxies look markedly different. The giant elliptical galaxy NGC 1407 has a core with nearly constant surface brightness, as was known from HST/ACS optical imaging (Spolaor et al. 2008). In contrast, the surface brightness of NGC 2695 peaks toward the

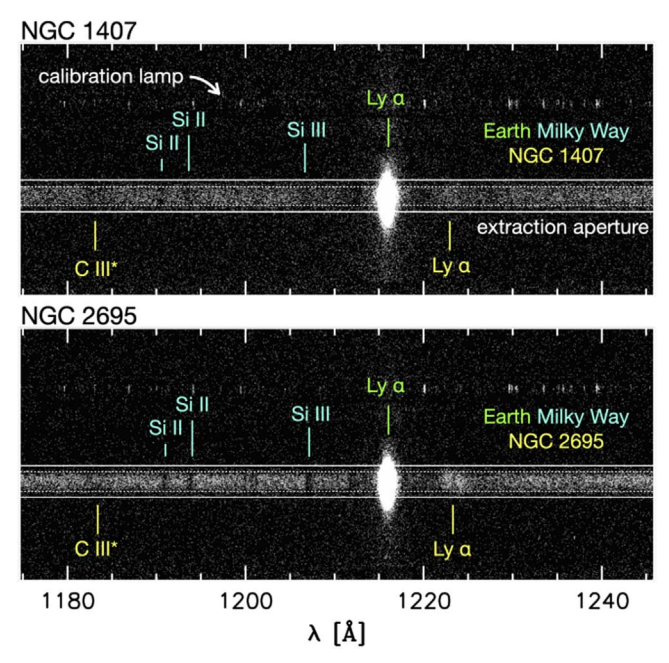


Figure 7. Small sections of the 2D spectra of NGC 1407 and NGC 2695 in the Ly α region. The pixel size is 0.12 Å in the wavelength direction and 0."11 in the spatial direction. Prominent features are marked, with geocoronal Ly α in green, Galactic lines in blue, and redshifted lines of the target galaxies in yellow. Horizontal dotted lines indicate the size of the 2."5 PSA. Solid lines indicate the (larger) extraction region, which contains 98% of the PSF-convolved flux through the PSA. The wavelength calibration lamp spectrum is also indicated

center, culminating in a bright nucleus. The area within r = 0.1125 is 1% of the total area of the PSA but contains 10% of the flux. We assess whether the nucleus is spatially resolved by comparing its spatial extent to that of the NUV images from the two acquisition images of the NGC 1407 offset star. The FWHM of the star is 0.1045, whereas the FWHM of the nucleus is 0.114. We infer that the nucleus of NGC 2695 is not a point source but has a half-light radius of ~ 0.11 , or ~ 20 pc. A decomposition of the point-spread function (PSF) corrected light profile of NGC 2695 is beyond the scope of this paper.

Two dispersing elements were used in the spectroscopic observations: the G130M grating in the first visit and the G160M grating in the second visit. The central wavelength for the G130M grating was set to $\lambda_{\text{cen}} = 1291 \text{ Å}$, giving a wavelength coverage for grating position FP-POS3 of $\Delta \lambda_{\rm B} = 1134-1274 \,\text{Å}$ for segment B and $\Delta \lambda_A = 1291-1431 \text{ Å}$ for segment A. For G160M these values are $\lambda_{\text{cen}} = 1533 \text{ Å}$, $\Delta \lambda_{\text{B}} = 1342-1515 \text{ Å}$, and $\Delta \lambda_{\rm A} = 1533 - 1707 \,\text{Å}$. With these settings the wavelength region 1342-1431 Å is covered by both gratings and therefore observed for the full four orbits. Within each visit the observations were split to dither in the wavelength direction. The G130M observations were split into two exposures at FP-POS3 and FP-POS4. The G160M observations were split into four, using all FP-POS positions. All spectroscopic exposures were obtained in TAGFLASH mode. In this mode the wavelength calibration lamp is periodically turned on, providing a timedependent wavelength solution that is used to compensate for drifts during the exposure.

3.3. Data Reduction, Calibration, and Galactic Extinction (Correction)

The observations were obtained in TIME-TAG mode, and the raw data products are event files. These are processed with the calcos pipeline, yielding flat-fielded flt files that in the STScI parlance are "intermediate calibrated output products." The final products of the pipeline are one-dimensional fluxcalibrated and wavelength-calibrated extractions from these flt files, but as these are only appropriate for point sources, we begin our analysis with the two-dimensional flt files. These files have two axes: a wavelength axis of 16,384 pixels with a pixel size of 0.012 Å, and a spatial axis of 1024 pixels with a pixel size of 0."114. The 2."5 aperture takes up only 22 of these 1024 pixels (slightly more when the PSF is taken into account). The spectrum of the wavelength calibration lamp is recorded ≈ 110 pixels away from the galaxy spectrum. The PSF in the spatial direction has a complex shape and is quite broad by HST standards, with FWHM = 1."1: COS was not designed for spatially resolved kinematics.

For each galaxy there are 12 flt files: two wavelengthdithered exposures in G130M, for segments A and B, and four dithered exposures in G160M for segments A and B. Most of the pixels in these files are zero (meaning that no event was recorded during the exposure) because of the small spectral bins and the faintness of the targets: as an example, in the NGC 1407 G130M spectrum 97% of the pixels are zero at the original resolution. The data in each segment are combined and binned in the wavelength direction by a factor of 10, averaging the counts in each bin. This binning does not degrade the spectral resolution in a meaningful way. COS is oversampled by a factor of ~ 7 , and the width of the spectral features is further broadened by the spatial extent of the galaxies within the PSA (for Galactic interstellar medium (ISM) lines) or the velocity dispersion of the galaxies (for stellar absorption lines and Ly α). The COS FUV continuum background is very low and dominated by the detector. The measured detector background is 1.8×10^{-6} (counts) s⁻¹ (pixel⁻¹, and this value was subtracted from the 2D binned data. A small section of the binned 2D spectrum of each galaxy is shown in Figure 7.

The most prominent feature is the geocoronal Ly α line, caused by resonant scattering of solar Ly α photons in Earth's exosphere. Its strength varies strongly with the Sun-Earth angle as seen from HST; it is saturated in all our exposures. The width of the line at each spatial position is determined by the cord length of the 2"5 PSA, the wings of the line-spread function of COS, and detector effects. Narrow absorption lines are from diffuse clouds in the Milky Way (see, e.g., Zheng et al. 2019). Their width is determined by the UV morphology of the galaxies in the PSA: as NGC 2695 is more compact than NGC 1407, the lines are narrower in the NGC 2695 spectrum (see the Appendix). Redshifted lines from the target galaxies are indicated in yellow: the $\lambda 1175.7$ C III complex and Ly α . The Ly α line is a combination of emission and very broad absorption; we disentangle these components in the next section.

One-dimensional spectra were extracted from the 2D data by summing along the spatial axis. The extraction aperture is 37 pixels, or 4."2. This aperture contains > 98% of the flux through the PSA, as determined both from direct measurements of the spatial profile and from a simulated profile created by convolving the PSA with the spatial line-spread function. At this stage the data were also binned by another factor of two in

⁷ Both galaxies and the offset star for NGC 1407 were observed with MIRRORA. However, the offset star for NGC 2695 was observed with MIRRORB, as it is very bright ($m_{\rm NUV}=17.2$). MIRRORB produces a strongly distorted PSF.

the wavelength direction to increase the signal-to-noise ratio (S/N). For each grating and each segment the wavelength calibration was obtained from the corresponding x1dsum table. The wavelength-dependent flux calibration was obtained by dividing the NET and FLUX values in the x1dsum table and multiplying the measured counts by this conversion factor. To avoid edge effects, the conversion factor was extrapolated slightly for each segment using a polynomial fit. Next, all four spectral regions (segments A and B of G130M and segments A and B of G160M) were combined into a single 1D spectrum for each galaxy. The spectra were sampled on a rest-frame wavelength grid of 1100–1700 Å with 0.2 Å bins (equivalent to $55 \,\mathrm{km \, s^{-1}}$ at 1100 Å and 35 km $\mathrm{s^{-1}}$ at 1700 Å), using a velocity of $1784 \,\mathrm{km \, s}^{-1}$ for NGC 1407 and a velocity of $1833 \,\mathrm{km \, s}^{-1}$ for NGC 2695. In the region of overlap between the A segment of G130M and the B segment of G160M the extracted spectra were averaged. The errors in the spectrum were determined empirically. The best-fit continuum (+) line model (see Section (4.1) was subtracted from the data, and the scatter in the residuals was determined in 15 Å bins using the biweight estimator (Beers et al. 1990). The error spectrum was created by a spline interpolation onto our output wavelength grid, ignoring bins that contain geocoronal lines.

The final step in the reduction process is a correction for Galactic extinction. The E(B-V) values are 0.060 for NGC 1407 and 0.015 for NGC 2695, using the Schlafly & Finkbeiner (2011) recalibration of the Schlegel et al. (1998) reddening map. The most widely used extinction curve is the Fitzpatrick (1999) form with $R_V = 3.1$, as this best reproduces the colors of stars in the Sloan Digital Sky Survey (SDSS; Schlafly & Finkbeiner 2011). The conversion from optical reddening to FUV extinction (R_{UV}) is inherently uncertain, as it is sensitive to the size distribution of dust grains in the diffuse ISM (Weingartner & Draine 2001). Fitzpatrick (1999) uses IUE satellite spectra of stars from Fitzpatrick & Massa (1990) to determine the shape of the Galactic extinction curve in the FUV. These stars are in directions of fairly high extinction, and several later studies have used GALEX photometry to constrain $R_{\rm UV}$ in regions of the sky with low E(B-V). The results from these studies are somewhat conflicting, as discussed in Salim & Narayanan (2020). Yuan et al. (2013) find that the observed extinction in the GALEX FUV band is significantly lower than expected from the reference Fitzpatrick (1999) curve, based on stellar photometry. Sun et al. (2018) suggest that $R_V \approx 3.35$ produces a better fit than $R_V = 3.1$. However, Peek & Schiminovich (2013) come to the opposite conclusion, finding that their model for the observed variation in the number counts of galaxies requires that the FUV extinction is on average a factor of ~ 1.3 higher than expected. They suggest that regions with the lowest dust columns may have a larger fraction of very small silicate grains.

Given that these studies fall on either side of Fitzpatrick (1999) and the IUE spectra extend further into the FUV than the GALEX bands, we adopt the standard Fitzpatrick curve (with $R_V = 3.1$) to correct the spectra for Galactic extinction and adopt an uncertainty of ± 0.5 to account for the systematic uncertainty. This error bar also takes regional variation in extinction into account: Schlafly et al. (2016) find that R_V varies by $\sigma(R_V) \approx 0.2$ in different lines of sight. With these choices, the extinction at the wavelength of Ly α is a factor of $1.78^{+0.33}_{-0.20}$ for NGC 1407 and $1.16^{+0.05}_{-0.03}$ for NGC 2695. This 19%

uncertainty for NGC 1407 and 4% uncertainty for NGC 2695 is included in the error on our final Ly α flux measurement.

The calibrated 1D spectra, corrected for extinction, are shown in Figure 8. Prominent features are marked, with geocoronal lines in green (Ly α and the O I triplet), ISM lines from diffuse gas in the Milky Way in blue (see Appendix), and stellar features from NGC 1407 and NGC 2695 in red. Both spectra are very blue in F_{λ} , indicating prominent UV upturns (Code & Welch 1979; Burstein et al. 1988).

Remarkably, these are, to our knowledge, the highestquality spectra of early-type galaxies in the Ly α region that have so far been taken with any telescope. COS has not been used previously for this kind of work, and neither has the Space Telescope Imaging Spectrograph (STIS). The lack of STIS FUV spectra of early-type galaxies is likely simply a matter of sensitivity: in the FUV, COS is 10-30 times more sensitive than STIS. The best published FUV spectra of early-type galaxies were seven spectra obtained with the Hopkins Ultraviolet Telescope (HUT) during the Astro-1 mission on Space Shuttle Columbia in 1990 and the Astro-2 mission on Space Shuttle Endeavour in 1995 (Ferguson et al. 1991; Brown) et al. 1997), as well as a single spectrum of NGC 1399 with the Far Ultraviolet Spectroscopic Explorer (FUSE; Brown et al. 2002). The FUSE spectrum was the first to unambiguously detect stellar absorption lines of early-type galaxies in the FUV. The HUT spectra cover a wavelength range of 820–1840 Å but with relatively low S/N and at a resolution of $\approx 1000 \text{ km s}^{-1}$ The NGC 1399 FUSE spectrum only covers wavelengths blueward of Ly α . We cannot directly compare the COS spectra to these previous observations, as NGC 1407 and NGC 2695 were not part of the samples.

4. Observed Ly α/i -band Flux Ratio

4.1. Measurement of the Ly α Flux

The Ly α emission line is clearly detected in both galaxies and well separated from the geocoronal line. This constitutes the first detection of Ly α emission in nonactive early-type galaxies. However, measuring its flux is not straightforward, as it sits "inside" the deep and wide Ly α absorption trough. Both the emission and absorption come from old stars, but not the same stars: the UV continuum, including the Ly α absorption, is likely that of extreme horizontal branch stars (Brown et al. 1997; Yi et al. 1998), whereas the Ly α emission likely comes from main-sequence stars and giants (see Section 2).

We model and subtract the continuum in order to isolate the Ly α emission. We use a set of synthetic stellar templates that were generated from 1D plane-parallel atmospheres in LTE as described in our previous work (Conroy & van Dokkum 2012a; Conroy et al. 2018). The templates have solar metallicity, $\log g = 4.5$, and effective temperatures ranging from $\sim 10,000$ to $\sim 35,000$ K and are shown in Figure 9. As is well known, the strength of Ly α absorption decreases with increasing temperature, going from A stars to O stars. Owing to the broad wings of the line, it is possible to model the Ly α absorption in the region of the Ly α emission (1212–1220 Å) from a fit to shorter and longer wavelengths. The continuum in the galaxies is fit

We certainly did not realize this when we wrote the HST proposal. We verified that our proposed observations of NGC 1407 and NGC 2695 would not be direct duplicates, but we had no idea that *no* early-type galaxies had been observed with COS. Our ignorance was probably for the best: we might not have submitted the proposal had we known, thinking that some aspect of the instrument made such observations impossible.

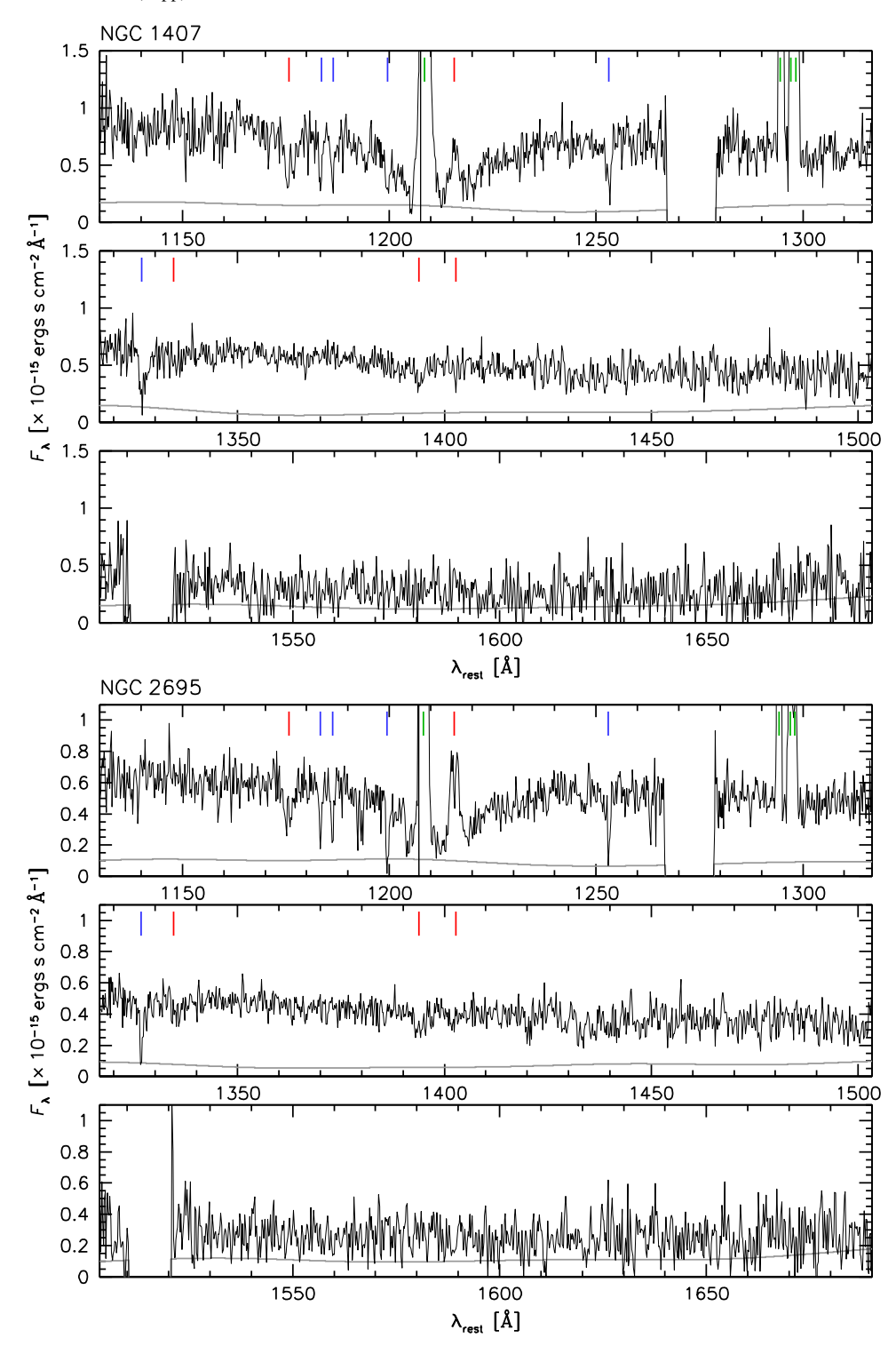


Figure 8. Calibrated and extinction-corrected 1D spectra of NGC 1407 and NGC 2695, sampled with a bin size of 0.2 Å. Geocoronal lines are marked in green, ISM lines from the Milky Way in blue, and stellar features from the two galaxies in red. The error spectrum is shown in gray.

with the following model:

$$(\mathbf{F}_{\mathbf{M}}) = \alpha_1 T_i + \alpha_2 T_j + \beta G, \qquad (2)$$

where T_i and T_j are distinct stellar templates and G is an approximate model for the Ly α emission. For NGC 1407 the model is a single Gaussian with $\lambda_{cen} = 1215.7$ Å and $\sigma = 1.18$ Å. For NGC 2695 the emission is modeled with two Gaussians, centered at 1215.1 and 1216.5 Å and each having

 $\sigma = 0.45$ Å. Narrow absorption lines and the geocoronal line are masked in the fit. The fit parameters are the discrete template identifiers i and j (each ranging from 1 to 8), α_1 , α_2 , and β .

The best-fitting model, obtained from a χ^2 minimization, is shown in Figure 10. The solid red line is the full fit, and the dotted line is $F_{\rm M} - \beta G$, that is, the stellar continuum model. We find that the two galaxies have slightly different stellar

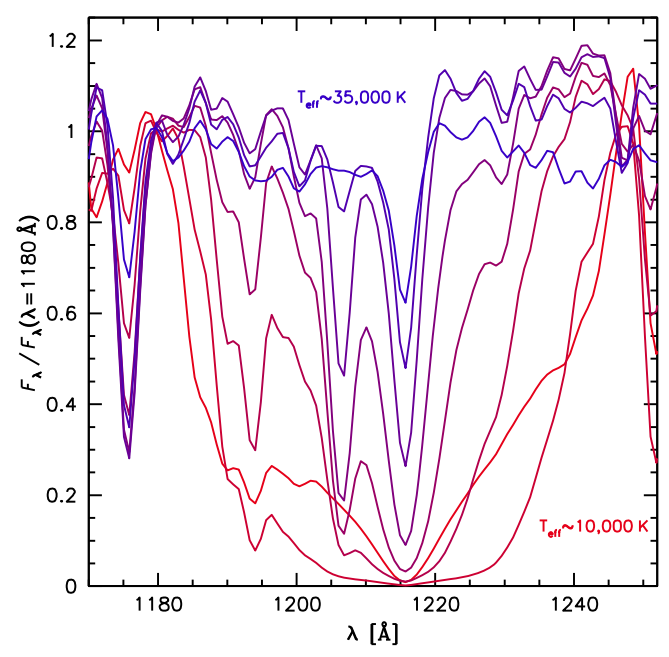


Figure 9. Synthetic stellar templates with $Z=Z_{\odot}$, $\log g=4.5$, and 10, 000 K < $T_{\rm eff}$ < 35,000 K that are used to model the continuum emission from hot horizontal branch stars in the Ly α region. The Ly α absorption is a strong function of temperature and affects a large spectral range from \sim 1185 to \sim 1240 Å.

continua in the Ly α region: NGC 2695 has weaker Ly α absorption than NGC 1407, suggesting that the mean temperature of the horizontal branch stars is somewhat higher in NGC 2695. This is not surprising, even in light of the very similar ages and abundances of these two galaxies, because the temperature distribution of the horizontal branch is known to be very sensitive to stellar parameters.

The stellar continuum models are subtracted from the spectra, and the residual spectra are shown in Figure 11. The Ly α emission from NGC 1407 and NGC 2695 can be easily identified and characterized in these spectra. We fit a linear function to the residual continuum. The Ly α emission is fit by a single Gaussian for NGC 1407 and a double Gaussian for NGC 2695. The two Gaussian components for NGC 2695 are assumed to have the same width and amplitude, as is expected to be the case if the emission comes from stars and the galaxy is in dynamical equilibrium. Errors are determined from simulations. In the simulations the best-fit models are perturbed with the empirically determined, wavelength-dependent errors and then refitted. The best-fitting models are shown by the red lines in Figure 11.

For NGC 1407 we find $\lambda_{\rm cen} = 1215.85 \pm 0.14 \, \text{Å}$, $\sigma = 1.49 \pm 0.15 \, \text{Å}$, and $F = (2.21 \pm 0.22) \times 10^{-15} \, \rm erg \, s^{-1} \, cm^{-2}$. The central (heliocentric) wavelength is equivalent to a velocity offset of $44 \pm 35 \, \rm km \, s^{-1}$, and we conclude that the central velocity of the Ly α (emission is consistent with the systemic velocity of the galaxy. The observed width of the line is larger than the intrinsic width owing to morphological line broadening. As the instrumental resolution $\sigma_{\rm instr} = 0.49 \, \, \text{Å}$ (see the Appendix), (the intrinsic width is $\sigma_{\rm intr} = 1.41 \pm 0.14 \, \, \text{Å}$, corresponding to $\sigma_{\rm intr} = 347 \pm 35 \, \, \text{km s}^{-1}$. For NGC 2695 the best-fitting parameters are $\lambda_{\rm cen,1} = 1215.06 \pm 0.07 \, \, \text{Å}$, $\lambda_{\rm cen,2} = 1216.50 \pm 0.06 \, \, \text{Å}$, $\sigma = 0.50 \pm 0.04 \, \, \text{Å}$, and $F = (1.51 \pm 0.09) \times 10^{-15} \, \rm erg \, s^{-1} \, cm^{-2}$. The averaged central wavelength is 1215.78 ± 0.07 , equivalent to a velocity offset of $27 \pm 17 \, \text{km s}^{-1}$ from the heliocentric radial

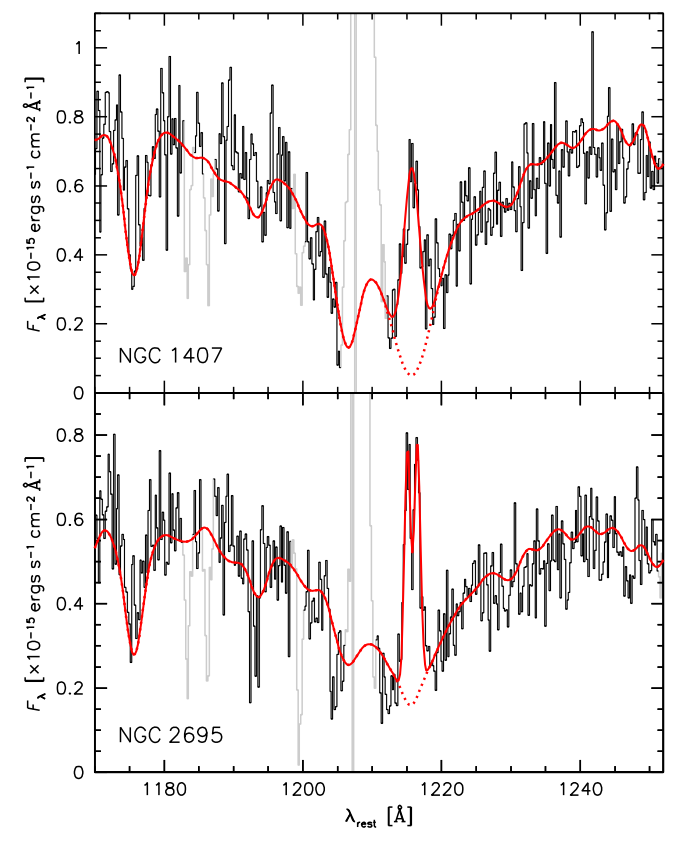


Figure 10. Continuum fit in the Ly α region, using linear combinations of the templates shown in Figure 9. Gray regions are masked in the fit. The Ly α emission from the galaxies is modeled with an ad hoc prescription (see text). The solid red line is the best-fitting model, and the dotted lines show the model without the Ly α emission component.

velocity of $1833 \pm 5 \,\mathrm{km \, s^{-1}}$. The velocity distance between the two components is $355 \pm 23 \,\mathrm{km \, s^{-1}}$, and as the instrumental resolution $\sigma_{\mathrm{instr}} = 0.33 \,\mathrm{\mathring{A}}$, (the intrinsic width of each of the components is $\sigma_{\mathrm{intr}} = 92 \pm 10 \,\mathrm{km \, s^{-1}}$.)

Adding the uncertainty in the Galactic extinction correction in quadrature to the random uncertainty, our final values for the Ly α emission line flux through the 2"5 diameter PSA are $F = (2.21 \pm 0.47) \times 10^{-15}$ erg s⁻¹ cm⁻² for NGC 1407 and $F = (1.51 \pm 0.11) \times 10^{-15}$ erg s⁻¹ cm⁻² for NGC 2695. We assume that this emission originates in stars and that no correction for H1 absorption needs to be applied. In the following subsection we use the 1D and 2D Ly α line profile to test this assumption.

4.2. Comparison to the Spatial Distribution and Kinematics of the Stars

The Ly α emission of a galaxy is often caused by the ionization and recombination of interstellar gas, as the line luminosity associated with this process can far exceed that of chromospheric activity (see, e.g., Ouchi et al. 2008). Although typical early-type galaxies are largely devoid of gas with $T \lesssim 10^5$ K, many have trace amounts of cold gas, dust, and warm gas in their central regions (van Dokkum & Franx 1995; Martini et al. 2003; Pandya et al. 2017), and some have active galactic nuclei (Kauffmann et al. 2003). Although neither galaxy shows evidence for dust in the NUV images (Figure 6), the possibility that the Ly α photons are largely or entirely originating in a gas disk cannot be discounted a priori. This is a

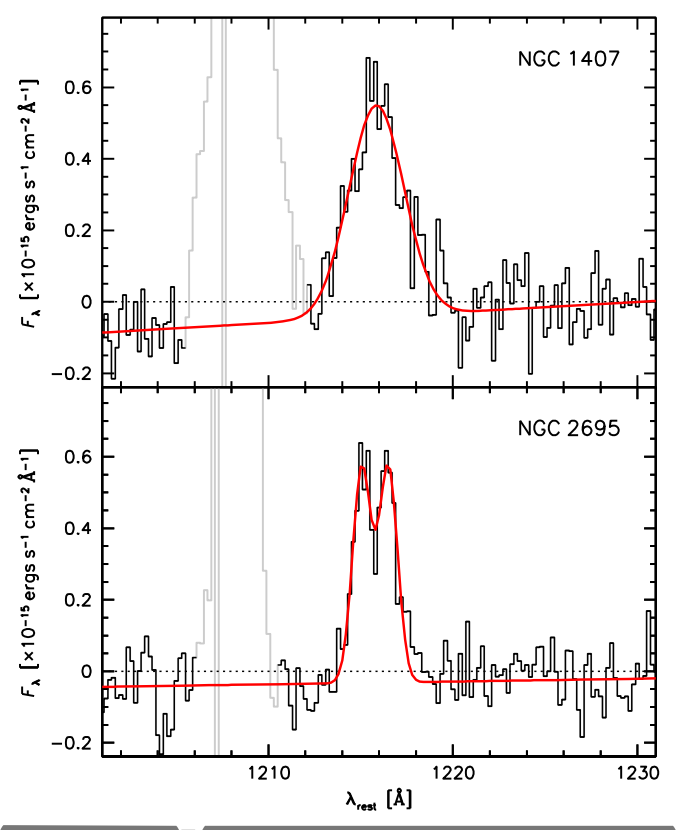


Figure 11. The Ly α emission of NGC 1407 and NGC 2695, obtained by subtracting the continuum models shown in Figure 10. The red lines are fits of Gaussians and a linear residual continuum correction. A single Gaussian is used for NGC 1407 and a double Gaussian for NGC 2695.

particular concern for NGC 2695, as its Ly α velocity profile is indicative of a disk. Unlike a slit, and analogous to a single-dish radio telescope, the circular aperture captures all velocity components in the central 2".5 but does not spatially resolve them. As a result, disk-like rotation produces a characteristic double-horned profile (see also Appendix C of van Dokkum et al. 2015, for the case of H α). Furthermore, Ly α photons are very easily absorbed by neutral hydrogen (Linsky et al. 2013). Here the concern is again for NGC 2695, as an alternative explanation for its double-peaked profile is that Ly α photons near the systemic velocity are preferentially absorbed, for instance, due to a face-on neutral hydrogen disk.

Fortunately, we can test whether or not the Ly α emission originates in stars by comparing the spatial distribution of Ly $\overline{\alpha}$ to that of the stellar continuum and by comparing the shape of the Ly α line to that of the stellar absorption lines. Although the stars producing the Ly α emission and the stars producing the continuum are in different evolutionary phases (with Ly α) from main-sequence stars and giants and the continuum from hot horizontal branch stars), they are all old, with their different locations in the H-R diagram just a reflection of small differences in their masses. Their spatial distribution and kinematics should therefore be identical, or at least very similar. By contrast, the spatial distribution of ionized gas in early-type galaxies is not likely to be identical to that of the stars. The Ly α intensity depends on the distribution of ionizing sources and the density of the gas. Furthermore, as gas is collisional and the dynamical times in the central region are only $\sim 10^7$ yr, it is expected to be dynamically decoupled from the stars (Sarzi et al. 2006).

The spatial distributions of the Ly α emission and the stars are determined by summing the flux in the wavelength direction; this yields the line profile along the spatial direction (the vertical direction in Figure 7). For Ly α we sum over 1214.2–1217.2 Å; for the stellar continuum we sum over the range 1230–1260 Å. Results are shown in Figure 12 (first and third panel from left). Ly α is in red and the stellar continuum in black. For reference, the expected spatial profile of a point source, as extracted from the *_profile data, is shown by the dashed line. Both galaxies are spatially resolved, with NGC 1407 having a larger extent than NGC 2695 as expected from the acquisition images (Figure 6). The spatial distributions of Ly α and the stellar continuum are identical within the uncertainties, for both galaxies.

The velocity profile of Ly α is measured from the 1D spectrum; it is the profile shown in Figure 11, with the linear residual continuum fit subtracted and wavelength converted to velocity. The stellar continuum absorption is obtained by averaging the four absorption features that are indicated in Figure 8: the $\lambda 1175.7$ C III complex, $\lambda 1334.5$ C II, and the $\lambda\lambda 1393.8$, 1402.8 Si II lines. Before averaging the line profiles, they were resampled on a velocity (rather than wavelength) grid. The Ly α kinematics are compared to the stellar kinematics in the second and fourth panels of Figure 12. For this comparison the Ly α emission profile was inverted to create a pseudo-absorption profile: $F_{\text{Ly}\alpha}^{\text{inv}} = 1 - nF_{\text{Ly}\alpha}$, with n a normalization parameter. The Ly α kinematics and stellar kinematics are consistent with each other within the uncertainties.⁹ The most straightforward interpretation for this close correspondence of both the spatial distribution and the kinematics is that the Ly α emission in these two galaxies comes from the stars themselves (that is, from their chromospheres).

The close correspondence of the Ly α and stellar profiles in Figure 12 also provides a qualitative constraint on the importance of absorption by neutral hydrogen in the galaxies. The local ISM (LISM) in the Milky Way absorbs $\sim 50\%$ or more of the stellar Ly α photons even on scales as small as \sim 10 pc (e.g., Wood et al. 2005). If H I is present in early-type galaxies, it is usually in a disk, and both spatially and dynamically distinct from the stars (Serra et al. 2012). Significant absorption of stellar Ly α photons would therefore alter the observed spatial distribution and kinematics of the Ly $\overline{\alpha}$ emission, so that they are no longer identical to the stellar continuum light. We also note that it is a priori unlikely that absorption plays a similarly large role in NGC 1407 and NGC 2695 as in the Milky Way. No HI has been detected in NGC 1407 to deep limits (Huchtmeier 1994). NGC 2695 has not been observed to similar depth, but early-type galaxies in groups and clusters are typically nearly devoid of neutral hydrogen (Serra et al. 2012).

4.3. Measurement of the Aperture-matched i-band Flux

We will present results in terms of the Ly α flux normalized by the *i*-band flux, in order to remove overall normalization effects. In order to compute the *i*-band flux, we use archival images of NGC 1407 and NGC 2695 to measure the *i*-band flux. For

Qualitatively, it is reassuring that the double-horned profile of the Ly \alpha emission of NGC 2695 is also seen in the stellar absorption profile. Interestingly, there is a hint of such a disk-like feature in the kinematics of NGC 1407 as well. It would be interesting to measure the velocity fields in the central 2"5 in these galaxies using AO-assisted IFU spectroscopy (see, e.g., Thomas et al. 2016).

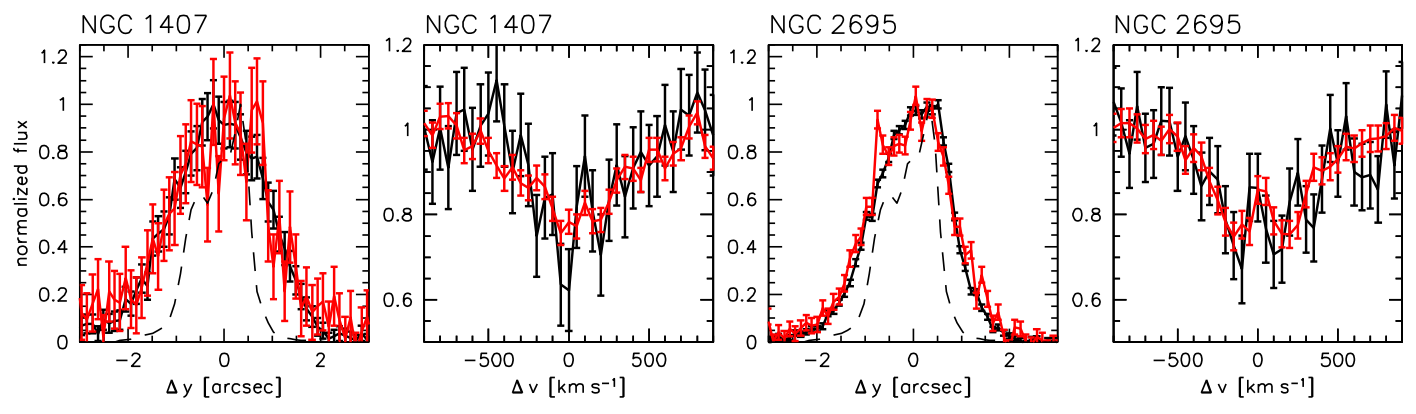


Figure 12. Comparison of the morphology and kinematics of the Ly α emission (red) to that of the stars (black). The first and third panels compare the distribution of Ly α along the spatial axis to that of the stellar continuum. For reference, the dashed line shows the spatial line-spread function of the COS FUV channel. The second and fourth panels compare the inverse of the Ly α velocity profile to the average absorption profile of four stellar lines. For both galaxies the Ly α emission traces both the spatial distribution and the kinematics of the stars.

Table 1 Measurements

| | $\alpha_{\mathrm{IMF}} (\mathrm{abs})^{\mathrm{a}}$ | $F(\text{Ly }\alpha)$ (10 ⁻¹⁵ erg s ⁻¹ cm ⁻²) | m ^a (mag) | $W_{\rm Ly \; \alpha}^{i} \ (10^{10} { m Hz})$ | $\alpha_{\rm IMF} \left(\text{Ly } \alpha \right)^{b}$ |
|----------|--|--|----------------------|---|---|
| NGC 1407 | $2.89^{+0.21}_{-0.19}$ | 2.21 ± 0.47 | 14.05 ± 0.06 | 2.5 ± 0.5 | 4.1 ± 1.1 |
| NGC 2695 | $1.94^{+0.22}_{-0.19}$ | 1.51 ± 0.11 | 13.69 ± 0.06 | 1.25 ± 0.12 | 1.5 ± 0.2 |

Notes

NGC 1407 we use Advanced Camera for Surveys (ACS) data in the F814W filter, obtained in the Cycle 11 program GO-9427 (PI: Harris). The galaxy was observed for 680 s, split into two 340 s exposures. NGC 2695 has not been observed in the optical with HST, and because of its bright center, it is saturated in most archival ground-based data sets (such as the Dark Energy Camera Legacy Survey). We use an *i*-band image obtained with the MegaPrime camera on the Canada–France–Hawaii Telescope in 2016 (PI: Duc). The image quality is excellent (with FWHM = 0″,56), and thanks to the short exposure time of 9 s, the center of the galaxy is not saturated.

The flux is measured through a circular aperture with a diameter of 2".5, corresponding to the size of the PSA. The throughput of the PSA is not uniform: light from $r \gtrsim 0$ ".6 is vignetted, such that the transmission at r = 1" is only $\approx 60\%$ of that in the center. On the other hand, light from beyond r = 1."25 enters the aperture owing to astigmatism of the beam. The net effect depends on the morphology of the galaxy. We find that for a range of profile shapes, parameterized by $I \propto e^{-\alpha r}$ with r in arcseconds and $0 < \alpha < 1$, the flux through an idealized 2".5 aperture is 101%–108% of the flux through the PSA. We take this into account by applying a downward correction of 5% to the measured i-band flux, with a 5% uncertainty.

Prior to measuring the flux of NGC 1407, the galaxy was convolved to the same spatial resolution as NGC 2695, and the sky that had been subtracted by AstroDrizzle was added back to the image (as it is nearly all galaxy light). Both steps have a $\lesssim 1\%$ effect on the measured flux. The F814W magnitude of NGC 1407 in the 2"5-diameter aperture is 14.11 ± 0.03 . Converting to the *i* band gives 14.12 ± 0.03 , and correcting for vignetting of the PSA gives 14.17 ± 0.06 . The Galactic extinction correction is 0.12 mag (Schlafly & Finkbeiner 2011), for a final measurement of $m_i = 14.05 \pm 0.06$. For NGC 2695

the measured *i*-band magnitude is 13.67 ± 0.04 , where the uncertainty takes into account any errors in the zero-point, (we verified that the nominal zero-point gives the correct magnitudes of SDSS stars to $\lesssim 3\%$). Correcting for vignetting and Galactic extinction of 0.03 mag gives $m_i = 13.69 \pm 0.06$. (Expressed in F_{ν} , (we have $F_{\nu}(i) = (8.7 \pm 0.5) \times 10^{-26}$ (erg s⁻¹ cm⁻² Hz⁻¹ for NGC 1407 and $F_{\nu}(i) = (1.21 \pm 0.07) \times 10^{-25}$ (erg s⁻¹ cm⁻² Hz⁻¹ for NGC 2695. Using the Ly α fluxes from Section 4.1, we find $W_{\rm Ly}^i = (1.25 \pm 0.12) \times 10^{10}$ (Hz for NGC 2695. For convenience we provide these measurements in Table 1.)

5. Comparison of Observations to Expectations

5.1. Ly α as a Measure of the IMF

The primary empirical result of this paper is that the normalized Ly α flux of NGC 1407 is higher than that of NGC 2695. This result is in the correct predicted sense given that our previous optical absorption-line analysis produced a steeper IMF for NGC 1407 compared to NGC 2695. These entirely independent methods both point to an excess of lowmass stars in NGC 1407 compared to NGC 2695. The ratio of the two values of $W_{\text{Ly} \alpha}^i$ is 2.0 \pm 0.4, and the difference between them is significant at the 99% level. The fact that these two galaxies have nearly identical stellar populations (at least within the observed aperture) disfavors any explanation for these observations that appeals to age or abundance differences. This study constitutes a classical hypothesis test; we are not attempting to find an explanation for an observation (in this case, a difference in Ly α fluxes between two galaxies), but rather are testing a prediction based on earlier work.

^a IMF parameter derived based on stellar population modeling of absorption-line spectra (van Dokkum et al. 2017).

^b IMF parameter derived based on $W_{\text{Ly}\,\alpha}^i$, using the "base + 0.2 dex" model.

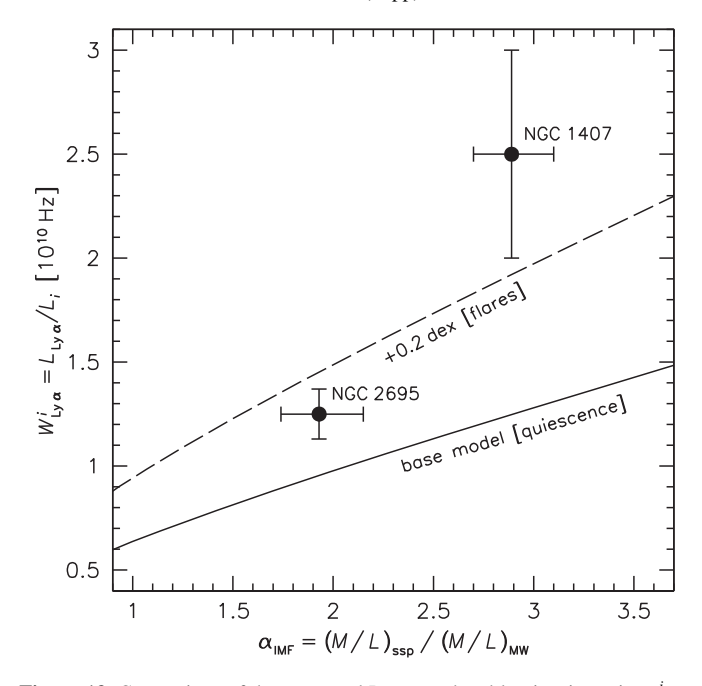


Figure 13. Comparison of the measured Ly α to *i*-band luminosity ratio $W_{\rm Ly}^i$ α for NGC 1407 and NGC 2695 to the model predictions of Section 2. The base model is for the quiescent state of all stars and is shown with a solid line. The dashed line accounts for the (likely maximum) effects of flares; here flares account for 37% of the time-averaged Ly α flux. The $\alpha_{\rm IMF}$ parameter is the mass excess compared to the IMF of the Milky Way, with $\alpha_{\rm IMF}=1$ representing a Kroupa (2001) IMF. The data fall in the same numerical range as the models, indicating that the COS observations are indeed measuring stellar activity and are consistent with the dashed line.

Somewhat to our surprise, the measured flux ratios are also in good *quantitative* agreement with expectations. In Figure 13 we compare the observed values of $W_{\rm Ly}^i{}_{\alpha}$ to the predictions of Section 2. For NGC 2695 we use the same value for $\alpha_{\rm IMF}$ as given in van Dokkum et al. (2017), $\alpha_{\rm IMF} = 1.93^{+0.22}_{-0.19}$, as that was for an aperture that is nearly identical to that used in the COS observations (\pm 1."2 along the slit, compared to the 2."5-diameter PSA). For NGC 1407 the value in van Dokkum et al. (2017; $\alpha_{\rm IMF} = 3.29$) corresponds to the central \pm 0."35. Instead, we use $\alpha_{\rm IMF} = 2.89^{+0.21}_{-0.19}$, which is the measurement within \pm 1."2. This difference likely partially reflects true radial variation in the galaxy (see Conroy et al. 2017), but it is also indicative of scatter between measurements that often exceeds expectations from the formal errors.

The data points are in the same numerical range as the model predictions, of a few \times 10^{10} Hz. That alone is remarkable: the models are based on a sparse set of Ly α observations of slowly rotating dwarfs and giants in the Milky Way, and the data are integrated-light observations in the centers of massive early-type galaxies. This is further evidence that the Ly α emission in NGC 1407 and NGC 2695 is indeed dominated by chromospheric activity on the surfaces of stars rather than, for example, recombination of ionized gas. Moreover, the data are consistent with a reasonable model, namely, a "base + 0.2 dex" model (see Section 2). The base model is for stars in the quiescent state. As discussed in Section 2, flares contribute significantly to the time- and population-averaged Ly α flux, with a plausible enhancement of 0.1–0.2 dex over the base model. The formal best fit to the two galaxies is for a 0.15 dex

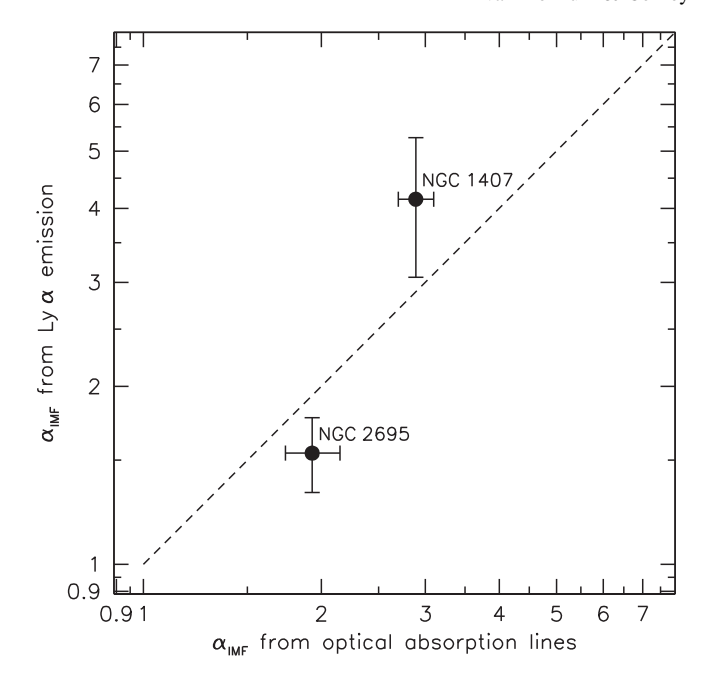


Figure 14. Comparison of the derived IMF parameter from Ly α to that derived from optical absorption lines. Here $W^i_{\rm Ly~\alpha}$ was converted to $\alpha_{\rm IMF}$ using the "base + 0.2 dex" model that includes the effects of flares (the dashed line in Figure 13). For both axes the error bars represent measurement uncertainties only and do not include systematic uncertainties in the stellar population synthesis modeling. A Kroupa (2001) IMF has $\alpha_{\rm IMF}=1$, and a Salpeter (1955) IMF has $\alpha_{\rm IMF}=1.5$.

enhancement, i.e., flares contributing about 30% of the total flux. The "base + 0.2 dex" model is also consistent with the data, with a probability of measuring the observed χ^2 of 11%. We note that the actual agreement is better, as model uncertainties and errors in $\alpha_{\rm IMF}$ are not accounted for in the χ^2 analysis (see Section 5.2).

Having established that the "base + 0.2 dex" model is a reasonable description of the data, we can present the results in a different way. The values of the IMF parameter that are implied by the observed $W_{\rm Ly~\alpha}^i$ ratio and the dashed line in Figure 13 are $\alpha_{\rm IMF} = 4.1 \pm 1.1$ for NGC 1407 and $\alpha_{\rm IMF} = 1.5 \pm 0.2$ for NGC 2695. In Figure 14 the two measurements of $\alpha_{\rm IMF}$, from Ly α emission and from gravity-sensitive absorption lines, are compared. The values are consistent at the $1\sigma - 2\sigma$ level. This is no surprise, as this plot is an alternative way to represent the information of Figure 13; the difference is that in Figure 14 we are not treating the Ly α measurement as the dependent variable.

5.2. Caveats and Limitations

The error bars do not include model uncertainties or systematic errors; they reflect observational errors only. There are several areas where the analysis can be improved. The model predictions are based on a small number of Milky Way dwarfs with poor sampling in the relevant age–temperature–metallicity space, and a larger number of old ($\sim 10~\rm Gyr$) stars would be very helpful. Furthermore, the question of how much flares contribute to the time- and population-averaged Ly α flux is uncertain, especially for old ages. Thankfully, there is considerable interest in understanding the flare rates in M dwarfs motivated by understanding the habitability of associated exoplanets (e.g., Segura et al. 2010; Shkolnik & Barman 2014; Shields et al. 2016; Loyd et al. 2018; Medina et al. 2020).

 $[\]overline{^{10}}$ We note that 0.2 dex is likely near the upper limit of the plausible effect of flares (see Section 2.2).

We have only considered chromospheric emission as a source of Ly α emission in old stellar systems. Any other emission source confined to evolved stars would result in an additive constant to our model predictions. For example, planetary nebulae (PNe) display strong emission lines, and they could be an additional source of Ly α flux. We use the PN specific frequency from Buzzoni et al. (2006) for elliptical galaxies and the universal [O III] luminosity function from Ciardullo (2010) to estimate a total [O III] luminosity per unit iband flux of 7×10^8 Hz. The ratio of Ly α to [O III] luminosity for PNe is empirically unconstrained, so we estimate this value using the Cloudy photoionization code (Ferland et al. 1998) and the "pn_paris_fast" PN model. The predicted Ly α -to-[O III] ratio is \sim 3, although we note that this depends sensitively on the assumed physical parameters of the source. This fiducial PN model predicts $W_{\text{Ly}\alpha}^{i} = 0.13 \times 10^{10} \text{ Hz}$, a factor of 10 lower than the observed value for NGC 2695. We therefore conclude that PNe are unlikely to contribute substantially to the Ly α luminosity in old stellar systems.

The observations also suffer from uncertainties. The IMF measurements from optical absorption lines have small formal uncertainties that likely underestimate the true error (see, e.g., Conroy & van Dokkum 2012a). This can be readily seen in the radial α_{IMF} profile of NGC 2695 in Figure 11 of van Dokkum et al. (2017). Turning to the Ly α measurements, the subtraction of the continuum emission (Section 4.1) can be improved with better models for the FUV emission of earlytype galaxies. The FUV extinction is a lingering uncertainty, particularly for NGC 1407 with its relatively high Galactic reddening E(B-V) = 0.06. The most concerning uncertainty is the possible presence of H I in the centers of the galaxies, as it is extremely efficient in absorbing Ly α photons. As is well known, many early-type galaxies have dust, and presumably associated HI, in the central few hundred parsecs (van Dokkum & Franx 1995; Martini et al. 2013). There is no hint of dust in the COS images in the NUV channel (see Figure 6), and the excellent correspondence between the spatial distribution and kinematics of the stars and the Ly α emission also suggests that absorption is not an issue, but we cannot exclude the presence of trace amounts of neutral HI. Extremely deep HI observations are needed to resolve this issue more definitively. Most of the other limitations can be overcome with larger samples.

6. Conclusions

In this paper we introduced a new way to measure the IMF in early-type galaxies that is complementary to other methods. While chromospheric activity is a stochastic and poorly understood process that is difficult to predict from fundamental principles, we have shown that it is possible to generate empirically motivated population-averaged predictions. The models predict very strong sensitivity of the integrated Ly α emission to the IMF-approximately 10× greater sensitivity than classic optical absorption-line analysis. We are greatly helped by a plethora of recent work (much of it with COS) on low-mass stars in the Milky Way in the context of the radiation environment of exoplanets (see, e.g., Loyd et al. 2018). On the observational side, COS proves to be well suited to the task of measuring the stellar Ly α emission in the centers of early-type galaxies. Here we are, of course, helped by the extraordinarily high density of stars in these regions, and also by the fact that this is

where IMF variations appear to be the strongest (Martín-Navarro et al. 2015; La Barbera et al. 2016; van Dokkum et al. 2017).

We predicted at the outset of this project that NGC 1407 would show a larger amount of chromospheric emission (per unit optical light) than NGC 2695—this is exactly what we observe. This result implies that NGC 1407 has a greater proportion of low-mass stars compared to NGC 2695, i.e., the IMF of NGC 1407 is more bottom-heavy than that of NGC 2695. This is in agreement with our previous work based on stellar population modeling of the optical-near-IR absorption-line spectra of these systems. Criticism of that previous work centered on the subtle signature in the data (1% - 2%)change in line depths) that could possibly be attributable to a variety of population-level effects. Any attempt to explain these two independent results as not being due to IMF variations must now explain the observed optical line depths and Ly α emission with a single mechanism (it is of course possible to appeal to two mechanisms-one for the optical and another for Ly α -but the IMF explanation then has the benefit of simplicity).

As noted in Section 5.2, the main avenue for improvement is in increasing the sample size. This is possible with a relatively modest investment of HST time, as only a few orbits per galaxy are needed. Larger samples will definitively address current limitations related to Galactic extinction corrections, possible H I absorption, and various model uncertainties. Furthermore, although this is not the subject of the present study, we note that the FUV spectra of early-type galaxies provide information on a wide array of other topics (see O'Connell 1999; Brown et al. 2002). Thanks to the superb sensitivity of COS, the spectra shown in Figure 8 are the best observations that have yet been obtained for early-type galaxies in this wavelength region, and as long as HST is operational, we can expect rapid progress in this area.

We thank the referee for helpful comments that improved the manuscript. C.C. thanks Dave Charbonneau for helpful conversations. Support from NASA grant HST-GO-15852 and the Packard Foundation is gratefully acknowledged.

Appendix Spectral Resolution

For spatially extended objects the line profile in the wavelength direction is essentially an image of the galaxy as observed through the aperture. As the circular 2".5-diameter PSA is a factor of ~50 larger than the spatial resolution delivered by HST, this morphological line broadening determines the spectral resolution even after binning the spectra by a factor of 20. The morphologies of NGC 1407 and NGC 2695 are quite different, with NGC 2695 having a much more peaked light distribution than NGC 1407 (see Figure 6). The spectral resolution of the NGC 2695 spectrum is consequently higher than that of the NGC 1407 spectrum.

The spectral resolution can be determined directly from the morphology. We collapse the NUV images in the *y*-direction (which is the spatial coordinate when the mirror is replaced by the grating) and convert the *x*-axis from arcseconds to wavelengths, taking the different pixel scales of the NUV and FUV detectors into account. We then compare the expected line broadening to the observed broadening of Galactic interstellar absorption lines. The average absorption profiles

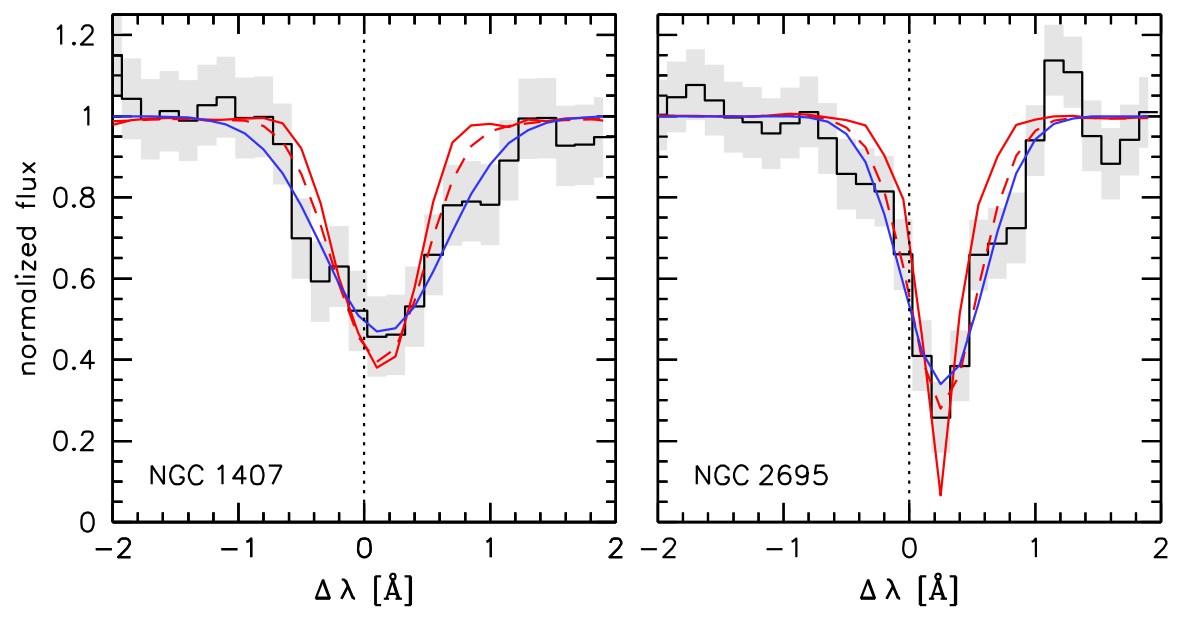


Figure 15. Average absorption profile of the four strongest Galactic ISM lines (indicated by blue markers in Figure 8). The lines are broadened by the light distribution of the galaxies in the PSA. Red lines are the expected profiles based on the morphologies of the galaxies, with the dashed profiles slightly smoothed versions of the solid profiles. Blue lines are Gaussian fits. The shifts of the lines reflect the velocities of the ISM clouds in the direction of the galaxies.

of the four strongest interstellar lines ($\lambda\lambda 1190.4$, 1193.3, 1260.3 Si II and $\lambda 1334.5$ C II) are shown in Figure 15. The red solid lines are the expected profiles from the NUV morphologies. The morphology provides a good description of the averaged NGC 1407 ISM line profile but is somewhat narrower than the NGC 2695 profile. This could be due to the resampling of the spectra or due to the intrinsic width and velocity structure of the cloud complexes toward NGC 2695. The red dashed lines are slightly smoothed (by 0.2 Å, or 1 rebinned pixel) versions of the red solid lines; they provide satisfactory fits for both galaxies. The blue lines are Gaussian fits to the observed averaged ISM profiles. The widths of the Gaussians are $\sigma_{\rm instr}=0.49$ Å for NGC 1407 and $\sigma_{\rm instr}=0.33$ Å for NGC 2695.

The heliocentric velocities of the ISM lines, \sim 21 km s⁻¹ for NGC 1407 and \sim 64 km s⁻¹ for NGC 2695, correspond to local standard of rest velocities of \sim 8 and \sim 48 km s⁻¹, respectively. These values are similar to typical velocities of Si IV absorption lines in QSO sight lines (Zheng et al. 2019).

ORCID iDs

References

```
Allen, M. J., Oluseyi, H. M., Walker, A. B. C., Hoover, R. B., & Barbee, T. W. 1997, SoPh, 174, 367
Astudillo-Defru, N., Delfosse, X., Bonfils, X., et al. 2017, A&A, 600, A13
Bastian, N., Covey, K. R., & Meyer, M. R. 2010, ARA&A, 48, 339
Beers, T. C., Flynn, K., & Gebhardt, K. 1990, AJ, 100, 32
Bezanson, R., van der Wel, A., Pacifici, C., et al. 2018, ApJ, 858, 60
Brown, T. M., Ferguson, H. C., Davidsen, A. F., & Dorman, B. 1997, ApJ, 482, 685
Brown, T. M., Ferguson, H. C., O'Connell, R. W., & Ohl, R. G. 2002, ApJL, 568, L19
Burstein, D., Bertola, F., Buson, L. M., Faber, S. M., & Lauer, T. R. 1988, ApJ, 328, 440
Buzzoni, A., Arnaboldi, M., & Corradi, R. L. M. 2006, MNRAS, 368, 877
Cappellari, M., McDermid, R. M., Alatalo, K., et al. 2012, Natur, 484, 485
```

```
Chabrier, G. 2003, PASP, 115, 763
Chamberlin, P. C., Eparvier, F. G., Knoer, V., et al. 2020, SpWea, 18, e02588
Chamberlin, P. C., Woods, T. N., Harder, J. W., Hock, R. A., & Snow, M.
  2008, AGU Fall Meeting Abstracts, SH21C-04
Choi, J., Dotter, A., Conroy, C., et al. 2016, ApJ, 823, 102
Chruślińska, M., Jeřábková, T., Nelemans, G., & Yan, Z. 2020, A&A,
  636, A10
Ciardullo, R. 2010, PASA, 27, 149
Code, A. D., & Welch, G. A. 1979, ApJ, 228, 95
Conroy, C., Gunn, J. E., & White, M. 2009, ApJ, 699, 486
Conroy, C., & van Dokkum, P. 2012a, ApJ, 747, 69
Conroy, C., & van Dokkum, P. G. 2012b, ApJ, 760, 71
Conroy, C., van Dokkum, P. G., & Villaume, A. 2017, ApJ, 837, 166
Conroy, C., Villaume, A., van Dokkum, P. G., & Lind, K. 2018, ApJ, 854, 139
Davis, T. A., & McDermid, R. M. 2017, MNRAS, 464, 453
Diamond-Lowe, H., Youngblood, A., Charbonneau, D., et al. 2021, AJ,
  162, 14
Esdaile, J., Glazebrook, K., Labbé, I., et al. 2021, ApJL, 908, L35
Ferguson, H. C., Davidsen, A. F., Kriss, G. A., et al. 1991, ApJL, 382, L69
Ferland, G. J., Korista, K. T., Verner, D. A., et al. 1998, PASP, 110, 761
Fitzpatrick, E. L. 1999, PASP, 111, 63
Fitzpatrick, E. L., & Massa, D. 1990, ApJS, 72, 163
France, K., Duvvuri, G., Egan, H., et al. 2020, AJ, 160, 237
France, K., Froning, C. S., Linsky, J. L., et al. 2013, ApJ, 763, 149
France, K., Loyd, R. O. P., Youngblood, A., et al. 2016, ApJ, 820, 89
Giampapa, M. S., & Liebert, J. 1986, ApJ, 305, 784
Hall, J. C. 2008, LRSP, 5, 2
Hopkins, P. F. 2012, MNRAS, 423, 2037
Huchtmeier, W. K. 1994, A&A, 286, 389
Joy, A. H., & Abt, H. A. 1974, ApJS, 28, 1
Kauffmann, G., Heckman, T. M., Tremonti, C., et al. 2003, MNRAS,
  346, 1055
Kiman, R., Faherty, J. K., Cruz, K. L., et al. 2021, AJ, 161, 277
Kroupa, P. 2001, MNRAS, 322, 231
Krumholz, M. R. 2011, ApJ, 743, 110
La Barbera, F., Ferreras, I., Vazdekis, A., et al. 2013, MNRAS, 433, 3017
La Barbera, F., Vazdekis, A., Ferreras, I., et al. 2016, MNRAS, 457, 1468
Linsky, J. L. 2017, ARA&A, 55, 159
Linsky, J. L., Bushinsky, R., Ayres, T., Fontenla, J., & France, K. 2012, ApJ,
  745, 25
Linsky, J. L., France, K., & Ayres, T. 2013, ApJ, 766, 69
Linsky, J. L., Wood, B. E., Youngblood, A., et al. 2020, ApJ, 902, 3
Loyd, R. O. P., France, K., Youngblood, A., et al. 2016, ApJ, 824, 102
Loyd, R. O. P., France, K., Youngblood, A., et al. 2018, ApJ, 867, 71
Lyubenova, M., Martín-Navarro, I., van de Ven, G., et al. 2016, MNRAS,
  463, 3220
```

```
Martini, P., Dicken, D., & Storchi-Bergmann, T. 2013, ApJ, 766, 121
Martini, P., Regan, M. W., Mulchaey, J. S., & Pogge, R. W. 2003, ApJ,
   589, 774
Martín-Navarro, I., Barbera, F. L., Vazdekis, A., Falcón-Barroso, J., &
  Ferreras, I. 2015, MNRAS, 447, 1033
Medina, A. A., Winters, J. G., Irwin, J. M., & Charbonneau, D. 2020, ApJ,
   905, 107
Mendel, J. T., Beifiori, A., Saglia, R. P., et al. 2020, ApJ, 899, 87
Milligan, R. O., Hudson, H. S., Chamberlin, P. C., Hannah, I. G., &
  Hayes, L. A. 2020, SpWea, 18, e02331
Newman, A. B., Belli, S., Ellis, R. S., & Patel, S. G. 2018, ApJ, 862, 126
Newman, A. B., Smith, R. J., Conroy, C., Villaume, A., & van Dokkum, P.
   2017, ApJ, 845, 157
O'Connell, R. W. 1999, ARA&A, 37, 603
Osten, R. A., Kowalski, A., Drake, S. A., et al. 2016, ApJ, 832, 174
Ouchi, M., Shimasaku, K., Akiyama, M., et al. 2008, ApJS, 176, 301
Pallavicini, R., Golub, L., Rosner, R., et al. 1981, ApJ, 248, 279
Pandya, V., Greene, J. E., Ma, C.-P., et al. 2017, ApJ, 837, 40
Peek, J. E. G., & Schiminovich, D. 2013, ApJ, 771, 68
Reiners, A., & Basri, G. 2007, ApJ, 656, 1121
Salim, S., & Narayanan, D. 2020, ARA&A, 58, 529
Salpeter, E. E. 1955, ApJ, 121, 161
Sarzi, M., Falcón-Barroso, J., Davies, R. L., et al. 2006, MNRAS, 366, 1151
Schlafly, E. F., & Finkbeiner, D. P. 2011, ApJ, 737, 103
Schlafly, E. F., Meisner, A. M., Stutz, A. M., et al. 2016, ApJ, 821, 78
Schlegel, D. J., Finkbeiner, D. P., & Davis, M. 1998, ApJ, 500, 525
Segura, A., Walkowicz, L. M., Meadows, V., Kasting, J., & Hawley, S. 2010,
   AsBio, 10, 751
Serra, P., Oosterloo, T., Morganti, R., et al. 2012, MNRAS, 422, 1835
Shields, A. L., Ballard, S., & Johnson, J. A. 2016, PhR, 663, 1
Shkolnik, E. L., & Barman, T. S. 2014, AJ, 148, 64
```

Skumanich, A. 1972, ApJ, 171, 565

```
Smith, R. J. 2014, MNRAS, 443, L69
Smith, R. J. 2020, ARA&A, 58, 577
Smith, R. J., Lucey, J. R., & Conroy, C. 2015, MNRAS, 449, 3441
Spiniello, C., Trager, S. C., Koopmans, L. V. E., & Chen, Y. 2012, ApJL,
  753, L32
Spolaor, M., Forbes, D. A., Proctor, R. N., Hau, G. K. T., & Brough, S. 2008,
  MNRAS, 385, 675
Sun, M., Jiang, B. W., Zhao, H., et al. 2018, ApJ, 861, 153
Thomas, J., Ma, C.-P., McConnell, N. J., et al. 2016, Natur, 532, 340
Toft, S., Zabl, J., Richard, J., et al. 2017, Natur, 546, 510
Treu, T., Auger, M. W., Koopmans, L. V. E., et al. 2010, ApJ, 709, 1195
van de Sande, J., Kriek, M., Franx, M., et al. 2013, ApJ, 771, 85
van der Wel, A., Rix, H.-W., Wuyts, S., et al. 2011, ApJ, 730, 38
van Dokkum, P., Conroy, C., Villaume, A., Brodie, J., & Romanowsky, A. J.
  2017, ApJ, 841, 68
van Dokkum, P. G., Brammer, G., Fumagalli, M., et al. 2011, ApJL, 743, L15
van Dokkum, P. G., & Conroy, C. 2010, Natur, 468, 940
van Dokkum, P. G., & Franx, M. 1995, AJ, 110, 2027
van Dokkum, P. G., Nelson, E. J., Franx, M., et al. 2015, ApJ, 813, 23
Vernazza, J. E., Avrett, E. H., & Loeser, R. 1981, ApJS, 45, 635
Weingartner, J. C., & Draine, B. T. 2001, ApJ, 548, 296
Wood, B. E., Müller, H.-R., & Harper, G. M. 2016, ApJ, 829, 74
Wood, B. E., Redfield, S., Linsky, J. L., Müller, H.-R., & Zank, G. P. 2005,
   ApJS, 159, 118
Woods, T. N., Chamberlin, P. C., Harder, J. W., et al. 2009, GeoRL, 36,
  L01101
Woods, T. N., Tobiska, W. K., Rottman, G. J., & Worden, J. R. 2000, JGR,
   105, 27195
Yi, S., Demarque, P., & Oemler, A. J. 1998, ApJ, 492, 480
Youngblood, A., France, K., Loyd, R. O. P., et al. 2016, ApJ, 824, 101
Yuan, H. B., Liu, X. W., & Xiang, M. S. 2013, MNRAS, 430, 2188
Zheng, Y., Peek, J. E. G., Putman, M. E., & Werk, J. K. 2019, ApJ, 871, 35
```